Computational Materials Science

Multi Defect Detection and Analysis of Electron Microscopy Images with Deep Learning

--Manuscript Draft--

Manuscript Number:	COMMAT-D-21-00154R1
Article Type:	Full Length Article
Section/Category:	Atomic Description
Keywords:	Deep Learning, Defect Detection and Analysis, Electron Microscopy, Faster R-CNN
Corresponding Author:	Dane Morgan University of Wisconsin-Madison Madison, WI UNITED STATES
First Author:	Mingren Shen
Order of Authors:	Mingren Shen
	Guanzhao Li
	Dongxia Wu
	Yuhan Liu
	Hima Bharathi Adusumilli
	Jacob Greaves
	Wei Hao
	Nathaniel J. Krakauer
	Leah Krudy
	Jacob Perez
	Varun Sreenivasan
	Bryan Sanchez
	Oigimer Torres
	Wei Li
	Kevin.G. Field
	Dane Morgan
Abstract:	Electron microscopy is widely used to explore defects in crystal structures, but human detecting of defects is often time-consuming, error-prone, and unreliable, and is not scalable to large numbers of images or real-time analysis. In this work, we discuss the application of machine learning approaches to find the location and geometry of different defect clusters in irradiated steels. We show that a deep learning based Faster R-CNN analysis system has a performance comparable to human analysis with relatively small training data sets. This study proves the promising ability to apply deep learning to assist the development of automated analysis microscopy data even when multiple features are present and paves the way for fast, scalable, and reliable analysis systems for massive amounts of modern electron microscopy data.
Response to Reviewers:	Prof. Susan Sinnott, Editor Computational Materials Science Dear Prof. Susan Sinnott, Thank you for your positive response and for allowing us to revise our manuscript titled “Multi Defect Detection and Analysis of Electron Microscopy Images with Deep Learning” (manuscript ID COMMAT-D-21-00154). We have carefully examined the reviewer’s comments and revised the manuscript accordingly as explained in the reply letter below. We hope that our response is sufficient to address all comments.

Listed below is a summary of changes made to the manuscript in response to the comments by the reviewer, as well as some additional edits made for clarification. The text changes are shown as highlighted text in the revised manuscript.

- We have added more information to explain the reason why we need new tools for defect analysis on Page 4 Line 50-55 of the revised manuscript.
- We have added the scale bar into Figure 1.
- We have corrected the link to the Figure 3.
- We have added discussion of error analysis of diameter difference and its relationship with defect density on Page 19-20 Line 290-304 of the revised manuscript.
- We have modified the text of model reproduction to clarify and include the aspects mentioned by the reviewer. The new text on the Page 20-21 line 311-323 of the revised manuscript.
- We have added one sentence about the default parameter used for CLAHE and Gaussian on Page 25 Line 406-408 of the revised manuscript.
- We have clarified the metric used for grid search of best parameter on Page 28 Line 464-465 of the revised manuscript.
- We have modified text to clarify what was done for watershed and ellipse fitting on Page 29 Line 481-488 of the revised manuscript.
- We have added typo of missing word “twice” for the black dot diameter definition on Page 30 Line 492 of the revised manuscript.
- We have proofread the text and equations and done our best to correct all the typos in the manuscript.

Best regards,

Mingren Shen, Guanzhao Li, Dongxia Wu, Yuhan Liu, Hima Bharathi Adusumilli, Jacob Greaves, Wei Hao, Nathaniel J. Krakauer, Leah Krudy, Jacob Perez, Varun Sreenivasan, Bryan Sanchez, Oigimer Torres, Wei Li, Kevin.G. Field, Dane Morgan

Corresponding author: Dane Morgan, E-mail: ddmorgan@wisc.edu

We thank the reviewers for their comments. We incorporated all the points raised by the reviewers in the revision, which are shown as highlighted text in the resubmitted manuscript document. Below we provide point-by-point responses (in black) to all questions of the reviewers (in blue) and descriptions of any changes to the manuscript. The page numbers refer to the revised manuscript.

Reviewer #2

Multi Defect Detection and Analysis of Electron Microscopy Images with Deep Learning

The authors present results to illustrate the quality of defect identification and property measurement in TEM micrograph images using a machine learning approach.
The work itself is well explained, with good choices made for comparison metrics, and the authors should be commended for making their data and models available.
I think the paper could benefit from tightening up the definitions of the metrics so that a quality comparison can be made between this method and others.
In some places, the enthusiasm for supervised learning shines through without some of the more cautious scientific caveats on reproducibility.
I have detailed below some places the authors might like to revisit.

We thank the reviewer for their supportive comments and detailed suggestions. Based on the comments below, we have revised the text related to metrics for clarity and tried to be more balanced in our discussion of the promise of supervised learning. Details are given in the point-by-point responses below.

Q1. Page 2
The authors state:
"many accurate and standardized data analysis tools [can] be effectively deployed, [none] can replace standard human analysis for identifying and locating defects"

This seems to be self-contradictory. Automated image analyses are routinely used. What are the cases that the authors have in mind where the current methods fail?

We agree with the reviewer that the text here is not clear and what we want to express here is that due to sample and imaging complexity, common automated tools may fail in edge cases or new material systems, so human efforts and hand-tunings are still needed which makes the data volume problem still hard to solve.

We have changed our description of Page 4 Line 50-55 into the following:

Not surprisingly, the EM community has developed many accurate image data analysis tools that can be effectively deployed to accommodate the large volume of EM data3,4. However, due to the complexity of images of material systems, these tools generally still need significant hand-tuning, and in some cases (like counting defects of irradiated materials), human identification of each defect is still the norm.

Q2. Page 6 image caption:

The scale in pixels might be useful here too given the context.

We have added the scale bar into Figure 1.

Q3. Page 9, description of the assessments

These assessments seem a very good set to compare the machine-labeling to human assessment, but as humans are fallible the set by itself does not give an objective quality measure.

Have the authors performed any tests against simulated data, where the ground truth is exactly and unambiguously known (for some geometrical quantities at least)?

Such tests would lend enormous weight to the power of the method, as well as making it easier for other groups to compare different methods in the future.

We agree with the reviewer that human labeling is not as objective as would be desired. We have not performed tests against simulated data for this type of loop defect data as no such simulated data exists, nor is there any easy path to obtain it. Simplified simulated data could be created (e.g., simple circles on a uniform background) but it would be impossible to assess how relevant any model results would be for real data. We are exploring methods to generate simulated data (e.g., using multi-slice methods and generative adversarial networks) but these are significant additional projects and there is always uncertainty about the impact of the necessary approximations. Therefore, we believe simulated data studies are best left to a later work where all the issues can be addressed and are beyond the scope of the present effort.

Q4. Page 9 para 2 and a few other places

There are some broken links "As shown in ., the red circles..."

We have corrected the link to the Figure, and it should be “As shown in Figure 3”.

Q5. Page 10, the cutoff for IoU

"As a compromise [] we used cutoff IoU = 0.4"

This value "feels" good for image 2 where the defects are densely packed, but poor for image 3 where the defects are well separated.

Q5a)

Is there a simple scaling for "good" performance in IoU based on e.g. homogeneous distribution density?

While there may be some theoretical justification for IoU values that can be derived from some kind of assumption of homogeneous density it is simpler and more common

in the community to base the result on actual performance vs. IoU, as in Figure 4 of the manuscript. A large IoU is ideal as it assures the best match between true and predicted bounding boxes. However, at some level, this requirement becomes unreasonable, and so we try to take the largest value that does not hurt performance significantly. We find this value as 0.4, which is similar to the standard 0.5 used in the computer vision community (For example, both ImageNet , COCO , and PASCAL , the three largest and widely used image datasets, evaluate object detection performance at a cut-off IoU = 0.5). Also, we note that the cut-off IoU 0.4 corresponds to a 57% overlapping area for two unit-size bounding boxes (x /(2-x) = 0.4 == > x = 4/7 ~ 0.57 as shown in the figure below), which is quite significant alignment.

Q5b)

Can the authors show examples of defect mismatches with IoU < 0.4, > 0.4? This would help readers less familiar with using this metric.

We are not totally sure what the reviewer means here but below we show three pairs of machine learning predicted (red) and ground truth (green) bounding box pairs with IOUs of (a) 0.221 (well below 0.4), (b) 0.402 (near 0.4), and (c) 0.624 (well above 0.4) to illustrate how they look. With a cutoff of 0.4 we would identify (a) as a false positive but (b) and (c) as successfully finding the defect. These results seem intuitively reasonable.

(a) (b) (c)

We are not sure how much these results would inform the general reader, so we have not added them to the manuscript.

Q6. Page 12, description of assessment 3.

Different human observers will categorize differently. Is there any research to indicate a confusion matrix comparable to table 3 for experienced human researchers? As it stands, I have no way of telling if the accuracies given (76%,87%,94%) are excellent, adequate, or hopeless.

The accuracy of human labeling is quite subtle to determine. It can depend sensitively on the system, the specific people, how much they communicate, how much time they spend, how many people check each result, etc. We have therefore not made any attempt to assess this value and view it as an important problem but outside the scope of this paper. Furthermore, we think the question of assessing the model accuracies should not hinge on the relative accuracies of different people. We think it is more important to assess the model in terms of whether the accuracies are adequate to yield physically useful information assuming the ground truth labeling is correct. We are clearly achieving this level of accuracy given the excellent mean size and areal densities we obtain. This paper is focused on assessing the accuracy of the model for reproducing our ground truth labeling. The challenge of obtaining accurate labeling in the community for training such models is an important topic but outside our scope.

Q7. Page 14, description of diameters

How is diameter defined? Particularly for the black-spot damage we could argue in favor of full-width-half maximum, or 95% rule, or...
The "mean" also needs defining - for an ellipse it could be the arithmetic or geometric average diameter, or those values averaged over the sample.

Perhaps the reviewer did not see the definition, but the diameter is defined on Page 29-30 Line 490-493 of the METHODS section as the following text shown

The diameters and areas of defects are defined as follows, where a and b are half the lengths of major and minor axes of the ellipse. The diameter of the a/2<111> and

a<100> defects are defined as 2a. The diameter of the black dot is defined as twice the square root of (ab).

We agree with the reviewers there might be different ways to define defects, but we think our approach is a reasonable one since all defects are 3D objects and the STEM images are just 2D projection of these 3D objects, so for more elliptical shape objects like a/2<111> and a<100> defects, 2a is a good characterization of its size since b is just a shortened by the projection of the loop being on an inclined plane and for more spherical objects like black dots, twice the square root of (ab) is a good approximation for its real size. And we thank the author since we found we missed the word twice (shown in red in original text) for black dots. This is corrected now, and all calculations are correct since we always comparing the diameter of the defect.

The mean size means the arithmetic mean of defect sizes, and we have added “arithmetic” to all the mean defect diameter discussion occurrences all over the manuscript.

Q8. Page 14, comparison of diameter performance

I don't think the case is really proved here.
Consider a ring with an intensity profile peaking at radius R, but with a line profile through the peak itself having a finite width r.
If r << R, we should be able to make a really accurate estimate of the radius R.
If r ~ R, the task is much harder. In a micrograph image we would be lucky to get a perfect circle with constant line profile, further complicating the issue.
Incautious fitting might easily lead to a case where the shape of the line profile inside and outside the maximum or noise leads to a systematic over or underestimate.

Q8a) How well does eg a Hough transform perform in the cases shown?

It is quite possible that a hand-tuned approach, e.g., a Hough transform could provide better performance on this particular data set and we do not mean to claim otherwise. However, such approaches are unable to tackle general defect detection in TEM images and would require impractically extensive hand tuning of hyperparameters for every dataset – in fact, this exact use case was the motivation of previous work in Ref. 5 of the revised manuscript. This fact cannot really be proven in any mathematical way, but we think that the ubiquitous use of hand labeling and the absence of any widely adopted automated defect detection tool in the radiation damage community is clear evidence that it is the case. The goal of this paper is to help develop a general tool for multiple class defect analysis that does not require extensive hand tuning for every new problem.

Q8b) How big is 2-9 pixels compared to the line profile?
This number of pixels is comparable (and in some cases less) to the thickness of defect loops. The ambiguity associated with the boundary region of the defects may create some of the observed noise.

We agree with the reviewer that finding a proper profile of the defects might help the detection of loops, but the case is more complicated than the ideal settings. Below we show one line profile of pixel intensity of an a<100> loop and this line is considered as the diameter of the loop and for this defect 2-9 is much smaller than the defect diameter.

Q9. Page 16: "2 pixels [error] is considered negligible in terms of impact on material properties."

This is not a valid statement.

We agree that this statement needed some qualification as it will depend on the defect sizes. To further clarify that the error is negligible for our defect population we have done a sensitivity analysis based on previous studies of hardening from loops. As discussed in Field et al. analysis shows for one of our alloys (Fe–Cr–Al alloys) the

hardening under irradiation from loops is

Now consider an error in diameter d defined as e. The fractional error in $\Delta\sigma y$ due to the error e is $\Delta\sigma yd+\varepsilon-\Delta\sigma yd\Delta\sigma yd\approx\varepsilon 2d$, where the approximate equality holds for \epsilon\ \ll\ d. For e = 1.7 nm (which is 2 pixels for our largest pixel sizes, see below) and d = 21.4 nm (our average sizes of a/2<111> and a<100> defects), we get the fractional error in $\Delta\sigma y$ as 1.7 nm / (2 * 21.4 nm) ≈ 0.04, which is well within the uncertainty of such microstructure-based analysis. However, for smaller defects this percentage error could clearly become larger. The error of diameter between ML results and human results appears to be approximately symmetrically distributed in positive and negative directions and independent of defect density, as shown in detail in SI section 4 and 5. However, for smaller defects this percentage error could clearly become larger. To address this issue with have added the following text to the manuscript on Page 19-20 Line 290-304:

To further clarify that the error is negligible for our defect population we have done a sensitivity analysis based on previous studies of hardening from loops. As discussed in Field et al. 31 simple dispersed barrier hardening models suggest that the hardening under irradiation from loops is of the form $\Delta\sigma y=A\ d$ where A is a constant and d is the diameter of the defect. Now consider an error in diameter d defined as . The fractional error in $\Delta\sigma y$ due to the error is $\Delta\sigma yd+\varepsilon-\Delta\sigma yd\Delta\sigma yd\approx\varepsilon 2d$, where the approximate equality holds for \epsilon\ \ll\ d. For = 1.7nm (which is 2 pixels for our largest pixel sizes, see below) and d = 21.4 nm (our average sizes of a/2<111> and a<100> defects), we get the fractional error in $\Delta\sigma y$ as 1.7 nm / (2 * 21.4 nm) ≈ 0.04, which is well within the uncertainty of such microstructure-based analysis. However, for smaller defects this percentage error could clearly become larger. The error of diameter between ML results and human results appears to be approximately symmetrically distributed in positive and negative directions and independent of defect density, as shown in detail in SI section 4 and 5.

Q9a How big is a pixel?

The pixel to nanometer ratio is from 0.14nm/pixel to 0.87nm/pixel as already discussed on Page 17 Line 258 of the manuscript.

Q9b is the error random or systematic?

The error is nearly random in the sense that is it not always high or low, nor does it show some unexpected groupings. As an illustration, below we show the diameter difference between ML and prediction for each class and shows that forms relatively symmetric and almost Gaussian looking distributions. Here we only considered those paired ground-truth labeling and ML prediction that are both correct in position prediction and defect type classification.

We have put the error analysis into SI section 4.

Q9c Is the error dependent on defect density?

We have examined the arithmetic mean of the error (ME), arithmetic mean of absolute value of the error (MAE), fractional ME (ME/ (arithmetic mean diameter of ground truth labeling), or FME) and fractional MAE (MAE/ (arithmetic mean diameter of ground truth labeling), or FMAE) in diameter for each of our 12 test images and plotted the values vs. the ground truth defect densities. The errors vs. density plots are shown below.

Figure 1. arithmetic mean of the error changes with the defect density

Figure 2. arithmetic mean of absolute value of the error changes with the defect density

Figure 3. (arithmetic mean of the error) / (arithmetic mean diameter of ground truth labeling) changes with the defect density

Figure 4. (arithmetic mean of absolute value of the error) / (arithmetic mean diameter of ground truth labeling) changes with the defect density

Figures 1 and 2 may show some trend of decreasing value with higher density, but we believe this is almost entirely due to the fact the low densities are correlated with larger loops, which lead to larger absolute errors. To correct for this aspect, we measure fractional (or percentage) errors, shown in Figure 3 and 4. These show no discernable trend with density. We therefore believe that there is no trend of error with density when the confounding effect of defect size is removed.

We have put the error dependence of density discussion into SI Section 5.

We have added the following text on Page 20 Line 301-304 of the revised manuscript.

The errors of diameter between ML results and human results appear to be approximately symmetrically distributed in positive and negative directions and independent of defect density, as shown in detail in SI section 4 and 5.

Q10. Page 16: "Once the model is properly trained, it will yield a unique and reproducible labelling for every image"

This is a difficult statement for me. It is trivially true that the analysis run a second time will give the same result.
But if the training set is added to, or is prepared by a different researcher, then it is not necessarily true.
The labelling is therefore not an algorithmic property of the images, and we should not expect other groups to be able to reproduce it starting from the images alone.
As the authors themselves point out "even the same person may label the same defects differently even after a short break."

We agree with the reviewers' points here and that the meaning of this statement is not clear. We have modified the text somewhat to clarify and include the aspects mentioned by the reviewer. The new text on the Page 20-21 Line 311-323 reads as the following,

While the exact performance of the present automated approach compared to different human researchers is difficult to determine rigorously there is no doubt that the present approach is much more consistent. Previous studies have shown that different labelers tend to label defects in different ways and even the same person may label the same defects differently even after a short break2,5. Such issues can make any given data analysis somewhat unreliable and make it difficult to integrate results across different teams and or time periods in larger analysis efforts. However, once a machine learning model is properly trained, it will yield a unique and reproducible labeling for every image. If the community could converge on a single or small number of models this could greatly increase the reproducibility in labeling of STEM experiments. That said, models trained on different data and/or different human labeling could give different predictions, so establishing community accepted models is an important part of using these approaches to obtain more consistent results.

Q11. Page 19: "The automated analysis [takes] about 0.1 s/image"

How does this value scale with pixel count or defect density?

The Faster R-CNN model will resize each image into 1024 pixel x 1024 pixel, which is also the pixel size of our TEM images, so the time to run object detection is not influenced by a higher number of pixels. However, downsizing an image with a higher

number of pixels will require extra time. We don't know the exact timing for this operation, and it could depend on many factors (e.g., machine speed, algorithms used, exact pixel count, etc.), but it is likely just tens of seconds at most for TEM images on a single processor. We, therefore, do not think it will be a significant issue. Assuming we use the same Faster RCNN hyperparameters the algorithm runs at approximately the same speed regardless of the number of defects in the image. If we have to alter the algorithm to use more proposal regions to detect more defects this could slow it down, but it is difficult to speculate on what would be necessary without detailed studies of the specific images.

Q12. Page 20: Data set preparation

Q12a. Any necessary parameters for CLAHE and Gaussian blur should be given explicitly.

The parameters used for CLAHE and Gaussian blur are all from the default parameter setting of scikit-images and the link to the detailed documentation of parameters used is put in the footnote.

We have added the text with two references of these parameters used on Page 25 Line 406-408 of the revised manuscript.

The parameters used for CLAHE45 and Gaussian blur46 are all from the default parameter setting of scikit-images and details can be found in the references given here for these methods.

Q12b. The use of additional filtered images in the RGB channels is a very neat idea. By how much does it actually help?

We do not have a direct assessment of the impact of adding different filtered images in the RGB channels. It is difficult to assess the model with just one channel as this would involve rewriting the basic Faster RCNN tools which take RGB as their standard input. We could provide the same images to each RGB channel, but this would require retraining the entire model, is a significant effort, and it is not clear how the separate channels would couple. Overall, we think it would be challenging to develop a rigorous and robust quantitative test to determine the impact of this particular choice of the training, and such testing is somewhat outside the main focus of the paper. We are therefore not adding any quantitative assessment of this approach relative to others and we would ask for the reviewer's understanding that there is limited time for such assessment. That said, we think the choice we have made of using different filtered images in the RGB channels is likely beneficial for the working of Faster R-CNN as it provides an additional way for data augmentation to make the model more robust to noise.

Q13. Page 24: "We used grid search [to find] the best choice of these two values."

How is "best" defined? Is this in terms of table 1,2,3 or a combination?

We selected the best values based on maximizing the F1 scores of the testing images, which is the F1 score shown in row 3 in Table 2. We have clarified this in the text on Page 28 Line 464-465.

Q14. Page 25: "Fitting the contour with an ellipse function"

How is the fitting done?

The overall fitting of the defect geometry is done in two steps. First, we use the watershed algorithm provided by OpenCV. The algorithm is applied to the cropped enlarged region of bounding boxes that contains the defect. We followed the official tutorial from OpenCV, and more details can be found there . Then the boundary from the Watershed algorithm was fit to an ellipse. Fitting with an ellipse was useful to match the approach used by the community, obtain a well-defined shape with simple geometric descriptors, and smooth out the otherwise rather rough boundaries found by the Watershed algorithm. OpenCV's fitEllipse() function was called to perform the fit.

	We have modified the mentioned text in the paper on Page 29 Line 481-488 to clarify what done for watershed and ellipse fitting, Watershed methods were applied to find the boundary between defect pixels and background pixels. We followed the official tutorial from OpenCV for performing the watershed and details of the approach can be found there50. We then fit the boundaries found from the Watershed algorithm to an ellipse. This fitting was done to match the approach used by the radiation defect analysis community, obtain a well-defined shape with simple geometric descriptors, and smooth out the otherwise rather rough boundaries found by the Watershed algorithm. The fitting was done with OpenCV's fitEllipse()function51.

Dear Editor,

We would appreciate your consideration of the enclosed manuscript:

Multi Defect Detection and Analysis of Electron Microscopy Images with Deep Learning

By Mingren Shen, Guanzhao Li, Dongxia Wu, Yuhan Liu, Hima Bharathi Adusumilli, Jacob Greaves, Wei Hao, Nathaniel J. Krakauer, Leah Krudy, Jacob Perez, Varun Sreenivasan, Bryan Sanchez, Oigimer Torres, Wei Li, Kevin.G. Field, Dane Morgan

for publication in *Computational Materials Science.*

Electron microscopy is one of the most widely used methods to explore and analyze defects in crystal structures, but when extensive defect identification and analysis is required the existing human-based analysis methods are time-consuming, error-prone, unreliable, and not scalable. It is therefore necessary to automate such analysis to make full use of the data available from modern electron microscopes.

In this work, we demonstrate a practical deep learning based model for automatic STEM image defect detection in irradiated nuclear steels. The model includes the Faster R-CNN module for detection and the watershed flood module for geometry fitting. The model improves significantly over similar previous similar efforts as it is simpler to train and is extended to multiple defect types. Our model performance is quite encouraging. Specifically, on three different defect types we achieved a F1 score of 0.78, and the predicted sizes and areal densities were very similar to the results obtained from previous human researchers.

Overall, we provide an accurate, efficient, reproducible, scalable, and extensible model to support counting of defects in STEM images of irradiated materials, and potentially many other systems. The model can be used to detect multiple types of defects (and potentially other features of the material) simultaneously. The model provides an important step in developing more automated STEM analysis. We believe this work will be of interest to the broad readership of Computational Materials Science and we sincerely hope you consider our paper for publication.

Best regards,
Mingren Shen, Guanzhao Li, Dongxia Wu, Yuhan Liu, Hima Bharathi Adusumilli, Jacob Greaves, Wei Hao, Nathaniel J. Krakauer, Leah Krudy, Jacob Perez, Varun Sreenivasan, Bryan Sanchez, Oigimer Torres, Wei Li, Kevin.G. Field, Dane Morgan

Corresponding author: Dane Morgan, E-mail: ddmorgan@wisc.edu

Prof. Susan Sinnott, Editor
Computational Materials Science

Dear Prof. Susan Sinnott,

Thank you for your positive response and for allowing us to revise our manuscript titled “Multi Defect Detection and Analysis of Electron Microscopy Images with Deep Learning” (manuscript ID COMMAT-D-21-00154). We have carefully examined the reviewer’s comments and revised the manuscript accordingly as explained in the reply letter below. We hope that our response is sufficient to address all comments.

Listed below is a summary of changes made to the manuscript in response to the comments by the reviewer, as well as some additional edits made for clarification. The text changes are shown as highlighted text in the revised manuscript.

- We have added more information to explain the reason why we need new tools for defect analysis on Page 4 Line 50-55 of the revised manuscript.
- We have added the scale bar into Figure 1.
- We have corrected the link to the Figure 3.
- We have added discussion of error analysis of diameter difference and its relationship with defect density on Page 19-20 Line 290-304 of the revised manuscript.
- We have modified the text of model reproduction to clarify and include the aspects mentioned by the reviewer. The new text on the Page 20-21 line 311-323 of the revised manuscript.
- We have added one sentence about the default parameter used for CLAHE and Gaussian on Page 25 Line 406-408 of the revised manuscript.
- We have clarified the metric used for grid search of best parameter on Page 28 Line 464-465 of the revised manuscript.
- We have modified text to clarify what was done for watershed and ellipse fitting on Page 29 Line 481-488 of the revised manuscript.
- We have added typo of missing word “twice” for the black dot diameter definition on Page 30 Line 492 of the revised manuscript.
- We have proofread the text and equations and done our best to correct all the typos in the manuscript.

Best regards,

Mingren Shen, Guanzhao Li, Dongxia Wu, Yuhan Liu, Hima Bharathi Adusumilli, Jacob Greaves, Wei Hao, Nathaniel J. Krakauer, Leah Krudy, Jacob Perez, Varun Sreenivasan, Bryan Sanchez, Oigimer Torres, Wei Li, Kevin.G. Field, Dane Morgan

Corresponding author: Dane Morgan, E-mail: ddmorgan@wisc.edu

We thank the reviewers for their comments. We incorporated all the points raised by the reviewers in the revision, which are shown as highlighted text in the resubmitted manuscript document. Below we provide point-by-point responses (in black) to all questions of the reviewers (in blue) and descriptions of any changes to the manuscript. The page numbers refer to the revised manuscript.

Reviewer #2

Multi Defect Detection and Analysis of Electron Microscopy Images with Deep Learning

The authors present results to illustrate the quality of defect identification and property measurement in TEM micrograph images using a machine learning approach.
The work itself is well explained, with good choices made for comparison metrics, and the authors should be commended for making their data and models available.
I think the paper could benefit from tightening up the definitions of the metrics so that a quality comparison can be made between this method and others.
In some places, the enthusiasm for supervised learning shines through without some of the more cautious scientific caveats on reproducibility.
I have detailed below some places the authors might like to revisit.

We thank the reviewer for their supportive comments and detailed suggestions. Based on the comments below, we have revised the text related to metrics for clarity and tried to be more balanced in our discussion of the promise of supervised learning. Details are given in the point-by-point responses below.

Q1. Page 2
The authors state:
"many accurate and standardized data analysis tools [can] be effectively deployed, [none] can replace standard human analysis for identifying and locating defects"

This seems to be self-contradictory. Automated image analyses are routinely used. What are the cases that the authors have in mind where the current methods fail?

We agree with the reviewer that the text here is not clear and what we want to express here is that due to sample and imaging complexity, common automated tools may fail in edge cases or new material systems, so human efforts and hand-tunings are still needed which makes the data volume problem still hard to solve.

We have changed our description of Page 4 Line 50-55 into the following:

> Not surprisingly, the EM community has developed many accurate image data analysis tools that can be effectively deployed to accommodate the large volume of EM data[3,4]. However, due to the complexity of images of material systems, these tools generally still

need significant hand-tuning, and in some cases (like counting defects of irradiated materials), human identification of each defect is still the norm.

Q2. Page 6 image caption:

The scale in pixels might be useful here too given the context.

We have added the scale bar into Figure 1.

Q3. Page 9, description of the assessments

These assessments seem a very good set to compare the machine-labeling to human assessment, but as humans are fallible the set by itself does not give an objective quality measure.

Have the authors performed any tests against simulated data, where the ground truth is exactly and unambiguously known (for some geometrical quantities at least)?

Such tests would lend enormous weight to the power of the method, as well as making it easier for other groups to compare different methods in the future.

We agree with the reviewer that human labeling is not as objective as would be desired. We have not performed tests against simulated data for this type of loop defect data as no such simulated data exists, nor is there any easy path to obtain it. Simplified simulated data could be created (e.g., simple circles on a uniform background) but it would be impossible to assess how relevant any model results would be for real data. We are exploring methods to generate simulated data (e.g., using multi-slice methods and generative adversarial networks) but these are significant additional projects and there is always uncertainty about the impact of the necessary approximations. Therefore, we believe simulated data studies are best left to a later work where all the issues can be addressed and are beyond the scope of the present effort.

Q4. Page 9 para 2 and a few other places

There are some broken links "As shown in ., the red circles..."

We have corrected the link to the Figure, and it should be “As shown in Figure 3”.

Q5. Page 10, the cutoff for IoU

"As a compromise [] we used cutoff IoU = 0.4"

This value "feels" good for image 2 where the defects are densely packed, but poor for image 3 where the defects are well separated.

Q5a)

Is there a simple scaling for "good" performance in IoU based on e.g. homogeneous distribution density?

While there may be some theoretical justification for IoU values that can be derived from some kind of assumption of homogeneous density it is simpler and more common in the community to base the result on actual performance vs. IoU, as in Figure 4 of the manuscript. A large IoU is ideal as it assures the best match between true and predicted bounding boxes. However, at some level, this requirement becomes unreasonable, and so we try to take the largest value that does not hurt performance significantly. We find this value as 0.4, which is similar to the standard 0.5 used in the computer vision community (For example, both ImageNet[1], COCO[2] , and PASCAL[3], the three largest and widely used image datasets, evaluate object detection performance at a cut-off IoU = 0.5). Also, we note that the cut-off IoU 0.4 corresponds to a 57% overlapping area for two unit-size bounding boxes (x /(2-x) = 0.4 == > x = 4/7 ~ 0.57 as shown in the figure below), which is quite significant alignment.

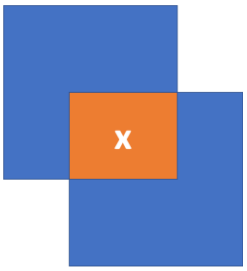

Q5b)

Can the authors show examples of defect mismatches with IoU < 0.4, > 0.4? This would help readers less familiar with using this metric.

We are not totally sure what the reviewer means here but below we show three pairs of machine learning predicted (red) and ground truth (green) bounding box pairs with IOUs of (a) 0.221 (well below 0.4), (b) 0.402 (near 0.4), and (c) 0.624 (well above 0.4) to illustrate how they look. With a cutoff of 0.4 we would identify (a) as a false positive but (b) and (c) as successfully finding the defect. These results seem intuitively reasonable.

---

[1] Russakovsky, Olga, Jia Deng, Hao Su, Jonathan Krause, Sanjeev Satheesh, Sean Ma, Zhiheng Huang et al. "Imagenet large scale visual recognition challenge." International journal of computer vision 115, no. 3 (2015): 211-252.

[2] Lin, Tsung-Yi, Michael Maire, Serge Belongie, James Hays, Pietro Perona, Deva Ramanan, Piotr Dollár, and C. Lawrence Zitnick. "Microsoft coco: Common objects in context." In European conference on computer vision, pp. 740-755. Springer, Cham, 2014.

[3] Everingham, Mark, SM Ali Eslami, Luc Van Gool, Christopher KI Williams, John Winn, and Andrew Zisserman. "The pascal visual object classes challenge: A retrospective." International journal of computer vision 111, no. 1 (2015): 98-136.

(a) 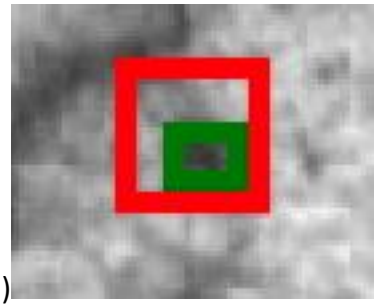 (b) 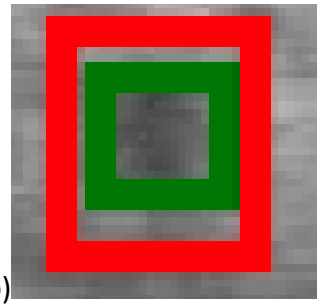 (c) 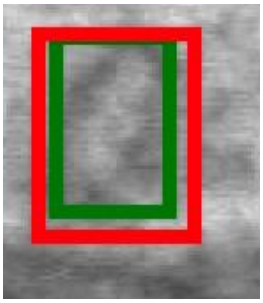

We are not sure how much these results would inform the general reader, so we have not added them to the manuscript.

Q6. Page 12, description of assessment 3.

Different human observers will categorize differently. Is there any research to indicate a confusion matrix comparable to table 3 for experienced human researchers? As it stands, I have no way of telling if the accuracies given (76%,87%,94%) are excellent, adequate, or hopeless.

The accuracy of human labeling is quite subtle to determine. It can depend sensitively on the system, the specific people, how much they communicate, how much time they spend, how many people check each result, etc. We have therefore not made any attempt to assess this value and view it as an important problem but outside the scope of this paper. Furthermore, we think the question of assessing the model accuracies should not hinge on the relative accuracies of different people. We think it is more important to assess the model in terms of whether the accuracies are adequate to yield physically useful information assuming the ground truth labeling is correct. We are clearly achieving this level of accuracy given the excellent mean size and areal densities we obtain. This paper is focused on assessing the accuracy of the model for reproducing our ground truth labeling. The challenge of obtaining accurate labeling in the community for training such models is an important topic but outside our scope.

Q7. Page 14, description of diameters

How is diameter defined? Particularly for the black-spot damage we could argue in favor of full-width-half maximum, or 95% rule, or...

The "mean" also needs defining - for an ellipse it could be the arithmetic or geometric average diameter, or those values averaged over the sample.

Perhaps the reviewer did not see the definition, but the diameter is defined on Page 29-30 Line 490-493 of the **METHODS section** as the following text shown

> *The diameters and areas of defects are defined as follows, where a and b are half the lengths of major and minor axes of the ellipse. The diameter of the a/2<111> and a<100>*

defects are defined as 2a. The diameter of the black dot is defined as ***twice*** *the square root of (ab).*

We agree with the reviewers there might be different ways to define defects, but we think our approach is a reasonable one since all defects are 3D objects and the STEM images are just 2D projection of these 3D objects, so for more elliptical shape objects like *a/2<111> and a<100> defects*, 2a is a good characterization of its size since b is just a shortened by the projection of the loop being on an inclined plane[4] and for more spherical objects like *black dots*, twice *the square root of (ab)* is a good approximation for its real size. And we thank the author since we found we missed the word twice (shown in red in original text) for black dots. This is corrected now, and all calculations are correct since we always comparing the diameter of the defect.

The mean size means the arithmetic mean of defect sizes, and we have added "arithmetic" to all the mean defect diameter discussion occurrences all over the manuscript.

Q8. Page 14, comparison of diameter performance

I don't think the case is really proved here.

Consider a ring with an intensity profile peaking at radius R, but with a line profile through the peak itself having a finite width r.

If r << R, we should be able to make a really accurate estimate of the radius R.

If r ~ R, the task is much harder. In a micrograph image we would be lucky to get a perfect circle with constant line profile, further complicating the issue.

Incautious fitting might easily lead to a case where the shape of the line profile inside and outside the maximum or noise leads to a systematic over or underestimate.

Q8a) How well does eg a Hough transform perform in the cases shown?

It is quite possible that a hand-tuned approach, e.g., a Hough transform could provide better performance on this particular data set and we do not mean to claim otherwise. However, such approaches are unable to tackle general defect detection in TEM images and would require impractically extensive hand tuning of hyperparameters for every dataset – in fact, this exact use case was the motivation of previous work in Ref. 5 of the revised manuscript. This fact cannot really be proven in any mathematical way, but we think that the ubiquitous use of hand labeling and the absence of any widely adopted automated defect detection tool in the radiation damage community is clear evidence that it is the case. The goal of this paper is to help develop a general tool for multiple class defect analysis that does not require extensive hand tuning for every new problem.

Q8b) How big is 2-9 pixels compared to the line profile?

[4] Yao, Bo, Danny J. Edwards, and Richard J. Kurtz. "TEM characterization of dislocation loops in irradiated bcc Fe-based steels." Journal of Nuclear Materials 434, no. 1-3 (2013): 402-410.

This number of pixels is comparable (and in some cases less) to the thickness of defect loops. The ambiguity associated with the boundary region of the defects may create some of the observed noise.

We agree with the reviewer that finding a proper profile of the defects might help the detection of loops, but the case is more complicated than the ideal settings. Below we show one line profile of pixel intensity of an *a<100> loop* and this line is considered as the diameter of the loop and for this defect 2-9 is much smaller than the defect diameter.

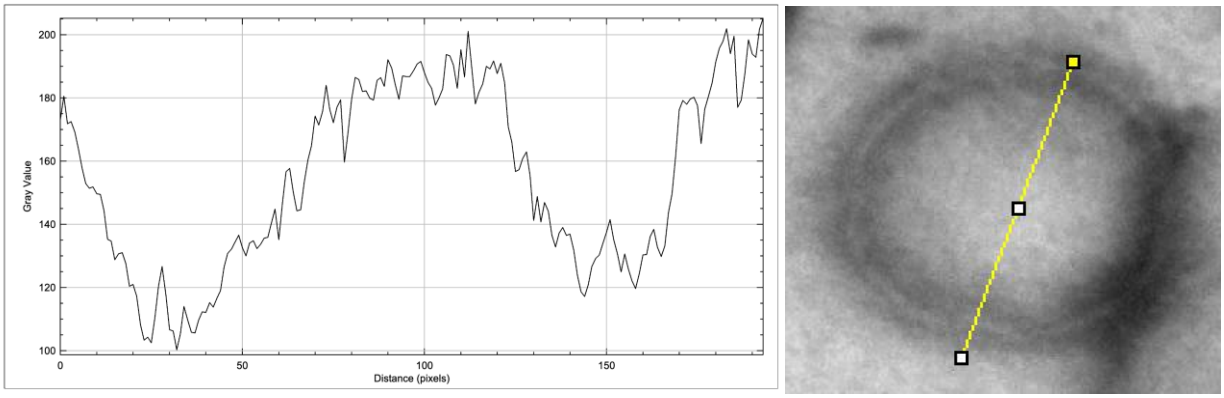

Q9. Page 16: "2 pixels [error] is considered negligible in terms of impact on material properties."

This is not a valid statement.

We agree that this statement needed some qualification as it will depend on the defect sizes. To further clarify that the error is negligible for our defect population we have done a sensitivity analysis based on previous studies of hardening from loops. As discussed in Field et al. analysis shows for one of our alloys (Fe–Cr–Al alloys[5]) the hardening under irradiation from loops is

$$\Delta\sigma_y = M\alpha\mu b\sqrt{\rho d} = A\sqrt{d}$$

Now consider an error in diameter *d* defined as *e*. The fractional error in $\Delta\sigma_y$ due to the error *e* is $\left(\Delta\sigma_y(d+\varepsilon) - \Delta\sigma_y(d)\right)/\Delta\sigma_y(d) \approx \varepsilon/(2d)$, where the approximate equality holds for $\epsilon \ll d$. For *e* = 1.7 nm (which is 2 pixels for our largest pixel sizes, see below) and *d* = 21.4 nm (our average sizes of a/2<111> and a<100> defects), we get the fractional error in $\Delta\sigma_y$ as 1.7 nm / (2 * 21.4 nm) ≈ 0.04, which is well within the uncertainty of such microstructure-based analysis. However, for smaller defects this percentage error could clearly become larger. The error of diameter between ML results and human results appears to be approximately symmetrically distributed in positive and negative directions and independent of defect density, as shown in detail in SI section 4 and 5. However, for smaller defects this percentage error could clearly

[5] Field, Kevin G., Xunxiang Hu, Kenneth C. Littrell, Yukinori Yamamoto, and Lance L. Snead. "Radiation tolerance of neutron-irradiated model Fe–Cr–Al alloys." Journal of Nuclear Materials 465 (2015): 746-755.

become larger. To address this issue with have added the following text to the manuscript on Page 19-20 Line 290-304:

> To further clarify that the error is negligible for our defect population we have done a sensitivity analysis based on previous studies of hardening from loops. As discussed in Field et al. [31] simple dispersed barrier hardening models suggest that the hardening under irradiation from loops is of the form $\Delta\sigma_y = A\sqrt{d}$ where A is a constant and d is the diameter of the defect. Now consider an error in diameter d defined as ε. The fractional error in $\Delta\sigma_y$ due to the error ε is $\left(\Delta\sigma_y(d+\varepsilon) - \Delta\sigma_y(d)\right)/\Delta\sigma_y(d) \approx \varepsilon/(2d)$, where the approximate equality holds for $\epsilon \ll d$. For ε = 1.7nm (which is 2 pixels for our largest pixel sizes, see below) and d = 21.4 nm (our average sizes of a/2<111> and a<100> defects), we get the fractional error in $\Delta\sigma_y$ as 1.7 nm / (2 * 21.4 nm) ≈ 0.04, which is well within the uncertainty of such microstructure-based analysis. However, for smaller defects this percentage error could clearly become larger. The error of diameter between ML results and human results appears to be approximately symmetrically distributed in positive and negative directions and independent of defect density, as shown in detail in SI section 4 and 5.

Q9a How big is a pixel?

The pixel to nanometer ratio is from 0.14nm/pixel to 0.87nm/pixel as already discussed on Page 17 Line 258 of the manuscript.

Q9b is the error random or systematic?

The error is nearly random in the sense that is it not always high or low, nor does it show some unexpected groupings. As an illustration, below we show the diameter difference between ML and prediction for each class and shows that forms relatively symmetric and almost Gaussian looking distributions. Here we only considered those paired ground-truth labeling and ML prediction that are both correct in position prediction and defect type classification.

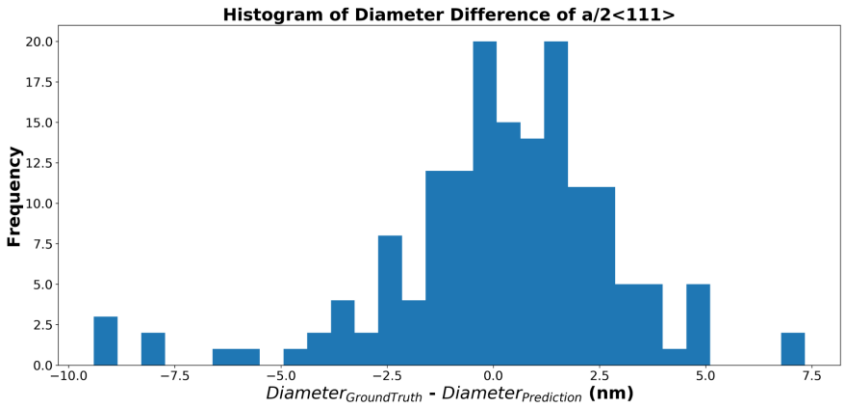

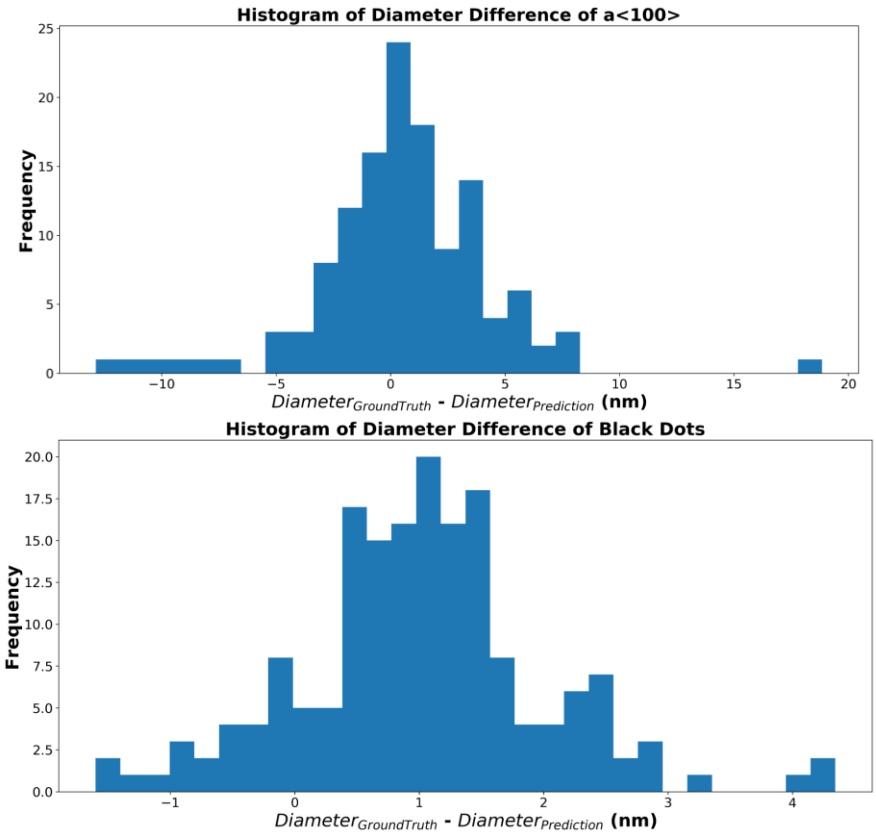

We have put the error analysis into SI section 4.

Q9c Is the error dependent on defect density?

We have examined the arithmetic mean of the error (ME), arithmetic mean of absolute value of the error (MAE), fractional ME (ME/ (arithmetic mean diameter of ground truth labeling), or FME) and fractional MAE (MAE/ (arithmetic mean diameter of ground truth labeling), or FMAE) in diameter for each of our 12 test images and plotted the values vs. the ground truth defect densities. The errors vs. density plots are shown below.

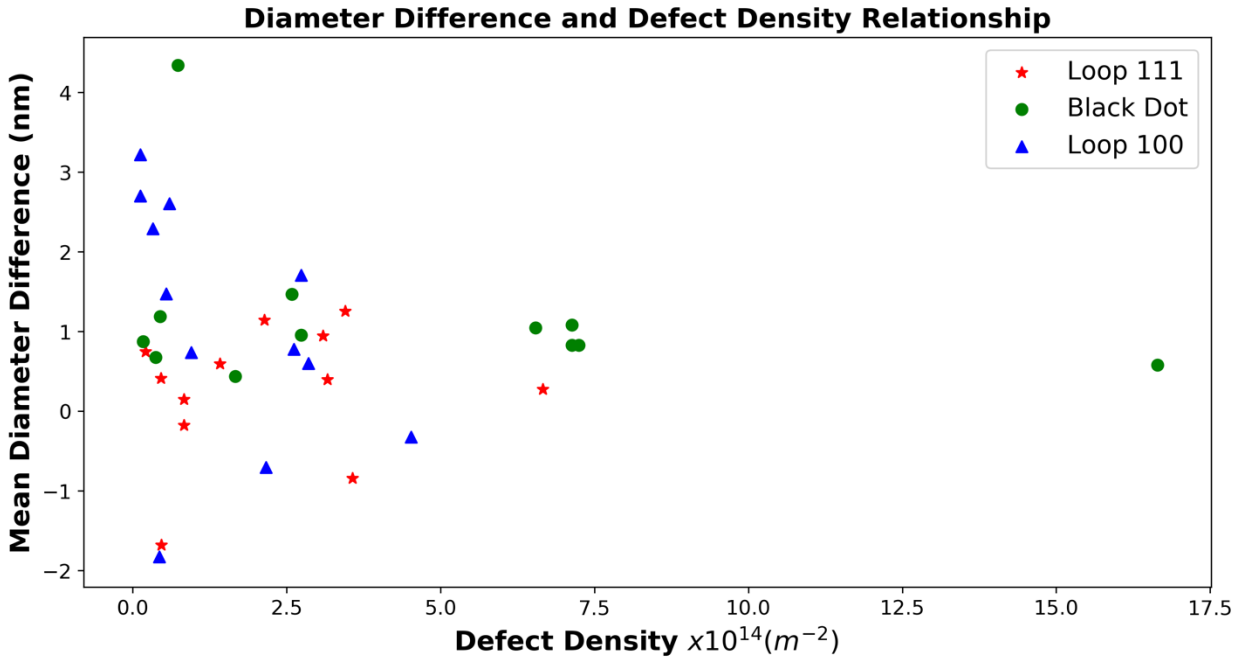

Figure 1. arithmetic mean of the error changes with the defect density

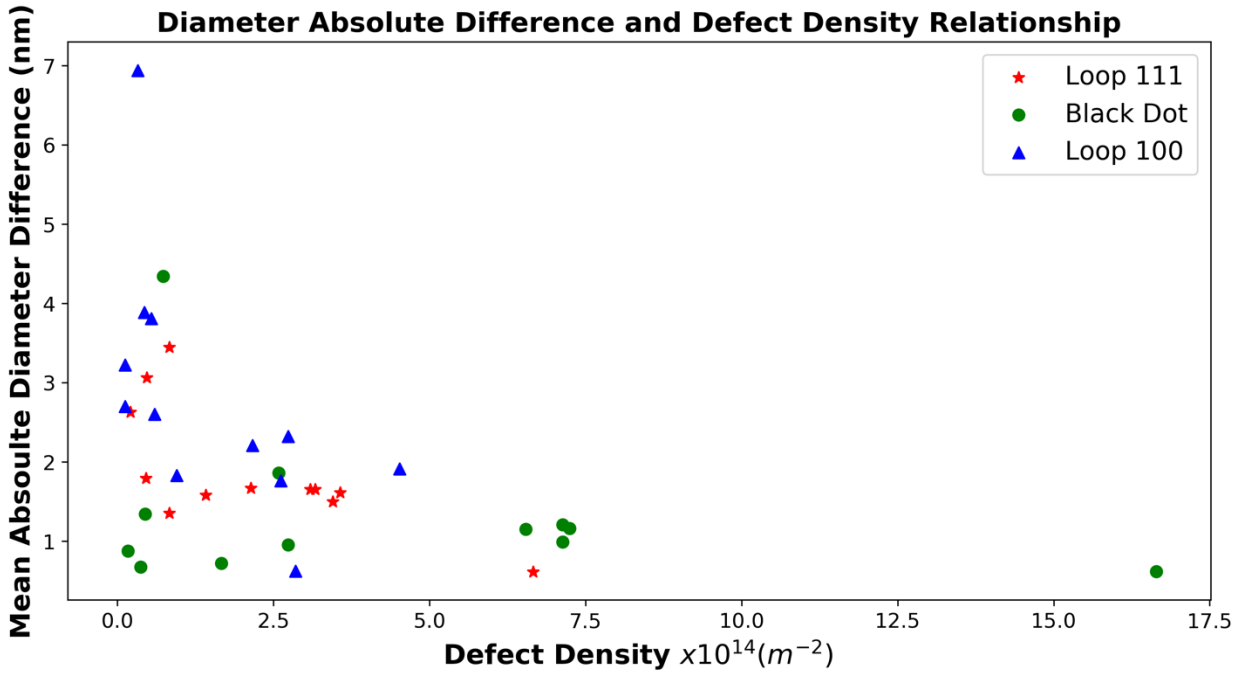

Figure 2. arithmetic mean of absolute value of the error changes with the defect density

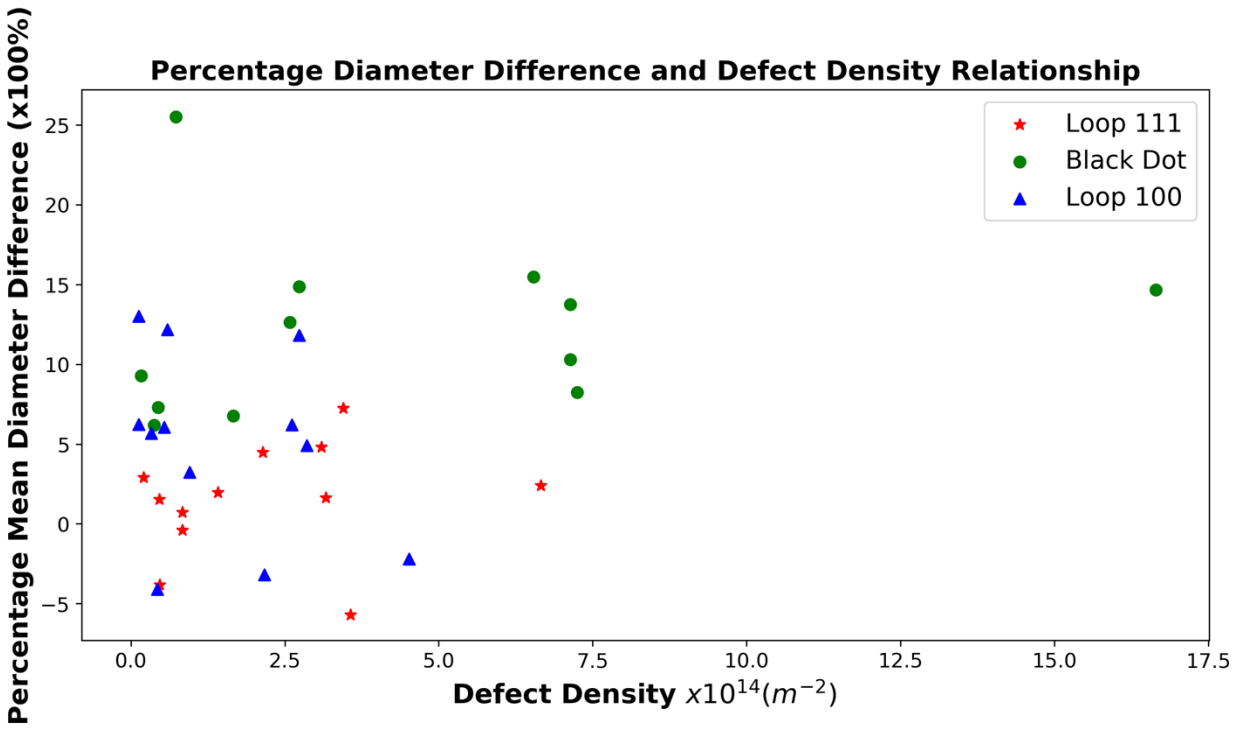

Figure 3. (arithmetic mean of the error) / (arithmetic mean diameter of ground truth labeling) changes with the defect density

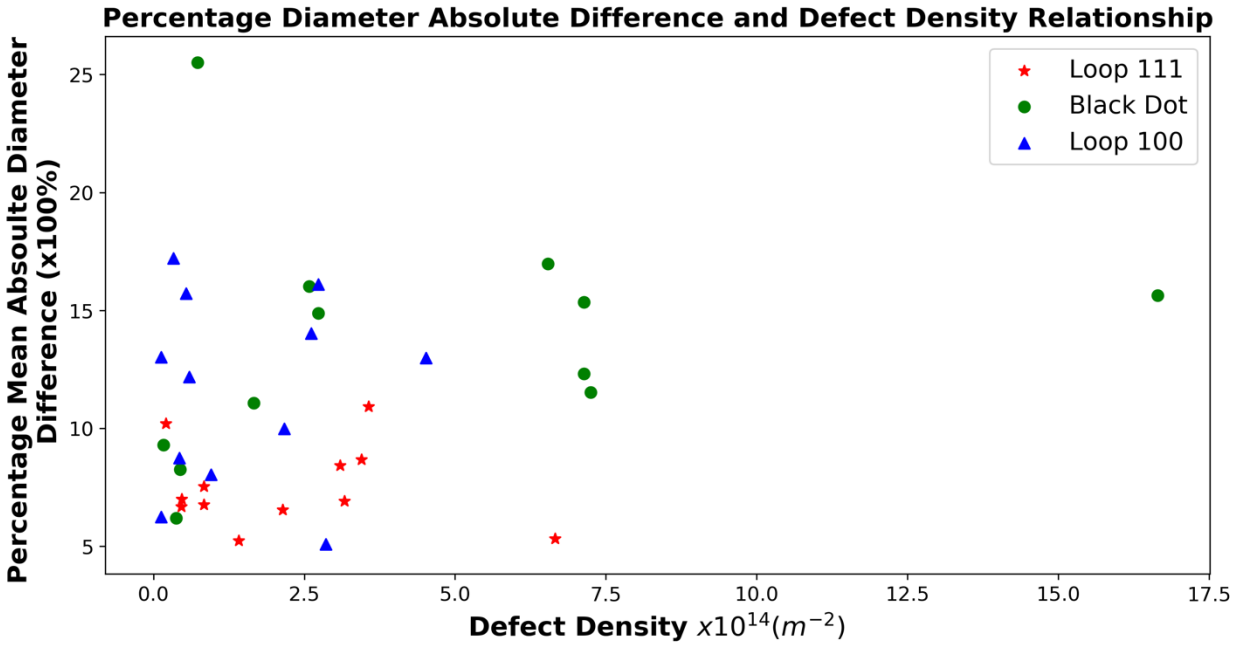

Figure 4. (arithmetic mean of absolute value of the error) / (arithmetic mean diameter of ground truth labeling) changes with the defect density

Figures 1 and 2 may show some trend of decreasing value with higher density, but we believe this is almost entirely due to the fact the low densities are correlated with larger loops, which

lead to larger absolute errors. To correct for this aspect, we measure fractional (or percentage) errors, shown in Figure 3 and 4. These show no discernable trend with density. We therefore believe that there is no trend of error with density when the confounding effect of defect size is removed.

We have put the error dependence of density discussion into SI Section 5.

We have added the following text on Page 20 Line 301-304 of the revised manuscript.

> The errors of diameter between ML results and human results appear to be approximately symmetrically distributed in positive and negative directions and independent of defect density, as shown in detail in SI section 4 and 5.

Q10. Page 16: "Once the model is properly trained, it will yield a unique and reproducible labelling for every image"

This is a difficult statement for me. It is trivially true that the analysis run a second time will give the same result.

But if the training set is added to, or is prepared by a different researcher, then it is not necessarily true.

The labelling is therefore not an algorithmic property of the images, and we should not expect other groups to be able to reproduce it starting from the images alone.

As the authors themselves point out "even the same person may label the same defects differently even after a short break."

We agree with the reviewers' points here and that the meaning of this statement is not clear. We have modified the text somewhat to clarify and include the aspects mentioned by the reviewer. The new text on the Page 20-21 Line 311-323 reads as the following,

> While the exact performance of the present automated approach compared to different human researchers is difficult to determine rigorously there is no doubt that the present approach is much more consistent. Previous studies have shown that different labelers tend to label defects in different ways and even the same person may label the same defects differently even after a short break[2,5]. Such issues can make any given data analysis somewhat unreliable and make it difficult to integrate results across different teams and or time periods in larger analysis efforts. However, once a machine learning model is properly trained, it will yield a unique and reproducible labeling for every image. If the community could converge on a single or small number of models this could greatly increase the reproducibility in labeling of STEM experiments. That said, models trained on different data and/or different human labeling could give different predictions, so establishing community accepted models is an important part of using these approaches to obtain more consistent results.

Q11. Page 19: "The automated analysis [takes] about 0.1 s/image"

How does this value scale with pixel count or defect density?

The Faster R-CNN model will resize each image into 1024 pixel x 1024 pixel, which is also the pixel size of our TEM images, so the time to run object detection is not influenced by a higher number of pixels. However, downsizing an image with a higher number of pixels will require extra time. We don't know the exact timing for this operation, and it could depend on many factors (e.g., machine speed, algorithms used, exact pixel count, etc.), but it is likely just tens of seconds at most for TEM images on a single processor. We, therefore, do not think it will be a significant issue. Assuming we use the same Faster RCNN hyperparameters the algorithm runs at approximately the same speed regardless of the number of defects in the image. If we have to alter the algorithm to use more proposal regions to detect more defects this could slow it down, but it is difficult to speculate on what would be necessary without detailed studies of the specific images.

Q12. Page 20: Data set preparation

Q12a. Any necessary parameters for CLAHE and Gaussian blur should be given explicitly.

The parameters used for CLAHE[6] and Gaussian blur[7] are all from the default parameter setting of scikit-images and the link to the detailed documentation of parameters used is put in the footnote.

We have added the text with two references of these parameters used on Page 25 Line 406-408 of the revised manuscript.

> The parameters used for CLAHE[45] and Gaussian blur46 are all from the default parameter setting of scikit-images and details can be found in the references given here for these methods.

Q12b. The use of additional filtered images in the RGB channels is a very neat idea. By how much does it actually help?

We do not have a direct assessment of the impact of adding different filtered images in the RGB channels. It is difficult to assess the model with just one channel as this would involve rewriting the basic Faster RCNN tools which take RGB as their standard input. We could provide the same images to each RGB channel, but this would require retraining the entire model, is a significant effort, and it is not clear how the separate channels would couple. Overall, we think it would be challenging to develop a rigorous and robust quantitative test to determine the impact of this particular choice of the training, and such testing is somewhat outside the main focus of the paper. We are therefore not adding any quantitative assessment of this approach relative to

[6] https://scikit-image.org/docs/stable/api/skimage.exposure.html#skimage.exposure.equalize_adapthist

[7] https://scikit-image.org/docs/dev/api/skimage.filters.html#skimage.filters.gaussian

others and we would ask for the reviewer's understanding that there is limited time for such assessment. That said, we think the choice we have made of using different filtered images in the RGB channels is likely beneficial for the working of Faster R-CNN as it provides an additional way for data augmentation to make the model more robust to noise.

Q13. Page 24: "We used grid search [to find] the best choice of these two values."

How is "best" defined? Is this in terms of table 1,2,3 or a combination?

We selected the best values based on maximizing the F1 scores of the testing images, which is the F1 score shown in row 3 in Table 2. We have clarified this in the text on Page 28 Line 464-465.

Q14. Page 25: "Fitting the contour with an ellipse function"

How is the fitting done?

The overall fitting of the defect geometry is done in two steps. First, we use the watershed algorithm provided by OpenCV. The algorithm is applied to the cropped enlarged region of bounding boxes that contains the defect. We followed the official tutorial from OpenCV, and more details can be found there[8]. Then the boundary from the Watershed algorithm was fit to an ellipse. Fitting with an ellipse was useful to match the approach used by the community, obtain a well-defined shape with simple geometric descriptors, and smooth out the otherwise rather rough boundaries found by the Watershed algorithm. OpenCV's `fitEllipse()` function[9] was called to perform the fit.

We have modified the mentioned text in the paper on Page 29 Line 481-488 to clarify what done for watershed and ellipse fitting,

> Watershed methods were applied to find the boundary between defect pixels and background pixels. We followed the official tutorial from OpenCV for performing the watershed and details of the approach can be found there[50]. We then fit the boundaries found from the Watershed algorithm to an ellipse. This fitting was done to match the approach used by the radiation defect analysis community, obtain a well-defined shape with simple geometric descriptors, and smooth out the otherwise rather rough boundaries found by the Watershed algorithm. The fitting was done with OpenCV's `fitEllipse()` function[51].

[8] https://docs.opencv.org/master/d3/db4/tutorial_py_watershed.html

[9] https://docs.opencv.org/master/d3/dc0/group__imgproc__shape.html#gaf259efaad93098103d6c27b9e4900ffa

Graphical Abstracts (for review)

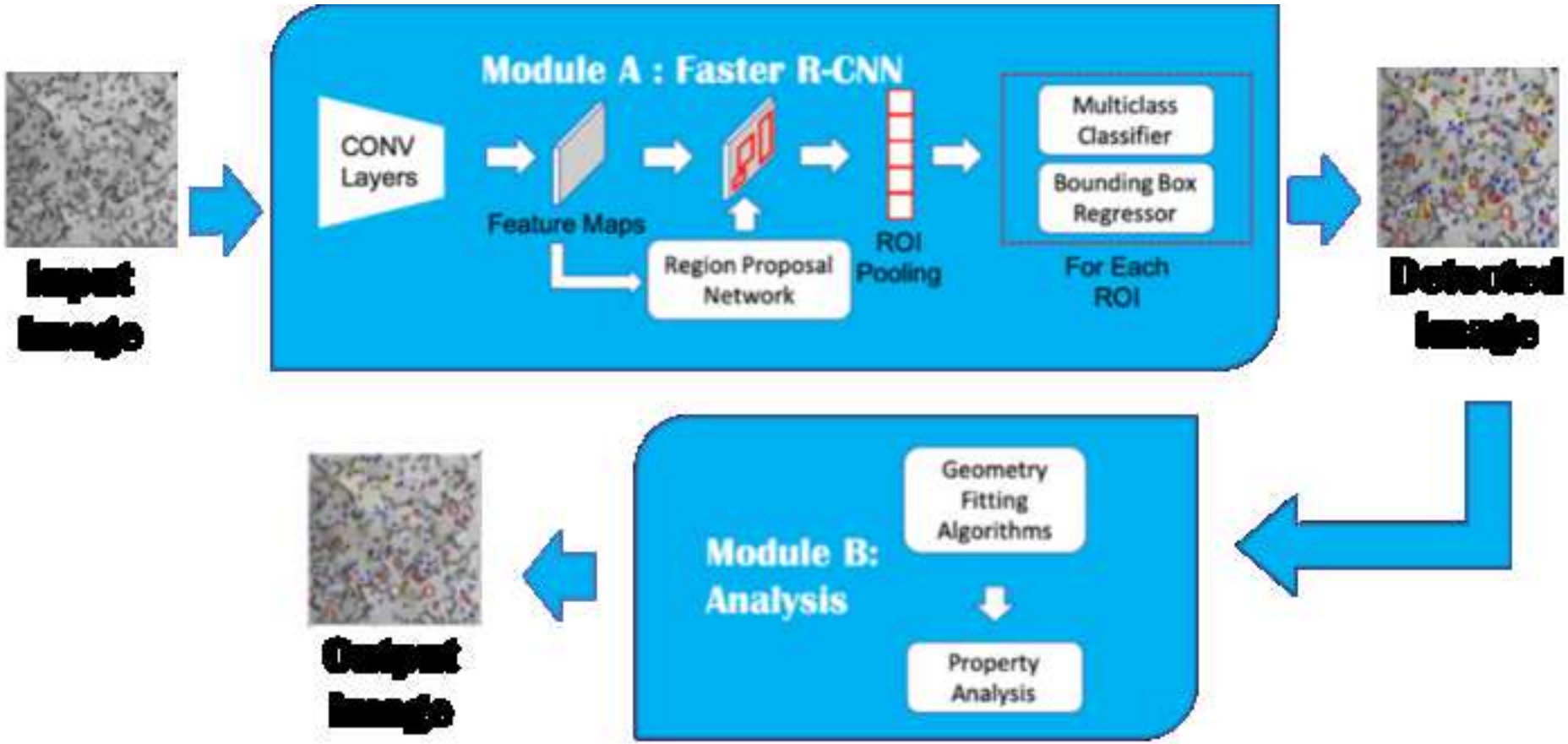

Multi Defect Detection and Analysis of Electron Microscopy Images with Deep Learning

Mingren Shen[1], Guanzhao Li[1], Dongxia Wu[9], Yuhan Liu[4], Hima Bharathi Adusumilli[8], Jacob Greaves[1], Wei Hao[4], Nathaniel J. Krakauer[4], Leah Krudy[5], Jacob Perez[4], Varun Sreenivasan[4], Bryan Sanchez[6], Oigimer Torres[7], Wei Li[3], Kevin.G. Field[2], Dane Morgan[1]

[1] Department of Materials Science and Engineering, University of Wisconsin-Madison, Madison, Wisconsin, 53706, USA

[2] Materials Science and Technology Division, Oak Ridge National Laboratory; Current address: Nuclear Engineering and Radiological Sciences Department, University of Michigan-Ann Arbor

[3] Google, Mountain View, California, 94043, USA

[4] Department of Computer Sciences, University of Wisconsin–Madison, Madison, Wisconsin, 53706, USA

[5] Department of Mathematics, Hope College, 141 E 12th Street, Holland Michigan, 49423, USA

[6] Department of Computer Science and Engineering, University of Puerto Rico at Mayagüez, Mayaguez, 00682, Puerto Rico

[7] Electrical and Computer Engineering Department, University of Puerto Rico at Mayagüez, Mayaguez, 00681, Puerto Rico

[8] Microsoft Corporation, Redmond, WA, 98052, USA

[9] Department of Mathematics, University of Wisconsin-Madison, Madison, Wisconsin, 53706, USA

Abstract

Electron microscopy is widely used to explore defects in crystal structures, but human detecting of defects is often time-consuming, error-prone, and unreliable, and is not scalable to large numbers of images or real-time analysis. In this work, we discuss the application of machine learning approaches to find the location and geometry of different defect clusters in irradiated steels. We show that a deep learning based Faster R-CNN analysis system has a performance comparable to human analysis with relatively small training data sets. This study proves the promising ability to apply deep learning to assist the development of automated analysis microscopy data even when multiple features are present and paves the way for fast, scalable, and reliable analysis systems for massive amounts of modern electron microscopy data.

INTRODUCTION

Electron microscopy (EM) is one of the most powerful tools for researchers to extract and collect micrometer down to angstrom scale structural and morphological properties of materials, including repeated structural units (e.g., unit cells of crystals) and defected regions (e.g., grain boundary, impurities, defect clusters). Traditionally, researchers have to manually label defects and repeatedly measure the relevant properties to obtain statistically meaningful values, which is time-consuming, error-prone, inconsistent, and hard to scale[1]. The issue of scaling has become pressing as increasing usage and advancement of EM techniques, such as high-speed detector and automated sample exploration in EM, now generate massive amounts of image data (e.g., up to thousands of images from a single experiment or condition can be generated in minutes) which will keep increasing in the near future[2]. Data on this scale cannot be practically examined by humans, and automated approaches are therefore now necessary to utilize the full power of modern EM. Not surprisingly, the EM community has developed many accurate image data analysis tools that can be effectively deployed to accommodate the large volume of EM data[3,4]. However, due to the complexity of images of material systems, these tools generally still need significant hand-tuning, and in some cases (like counting defects of irradiated materials), human identification of each defect is still the norm.

Well-designed and well-tested automated analysis has proven to be significantly more efficient, repeatable, and standardized than human analysis for discrete cases[2,4,56]. Developing automatic methods for EM image processing has drawn a great deal of interest in the material science community. Automation efforts typically rely on traditional computer vision technology, such as variance hybridized mean local thresholding[7], texture representation, and template matching methods like bag of visual words (BoW)[8,9], key-point matching methods[10,11], Hessian-based Blob boundary detection methods[12] and sometimes obtain better performance[13,14] by utilizing tools from broader areas, such as incorporating synthetic image dataset[15] and using machine learning methods like support vector machine[16] and k-means clustering[2]. However, these efforts typically require extensive human tuning and/or are limited to specific tasks.

Recent developments (<10 years) in deep learning methods[17,18] have demonstrated that object detection in images can be automated with minimal hyperparameters and yield human or even better than human levels of performance. These frameworks are now being adapted towards finding defects in metals, and particularly nuclear materials, including the automated detection of dislocation loops, cavities, precipitates, and line dislocations[5,19–21]. Generally, there are three different approaches for applying deep learning frameworks to defect detection in microscopy images. The first is using the combination of both traditional techniques and deep learning tools[5], for example, Li et al. develops an analysis model that includes a local

visual content descriptor widely used in computer vision called Local Binary Patterns (LBP)[22] descriptor, feature selecting methods called AdaBoost[23], and Convolutional Neural Network (CNN) module to screen candidate bounding boxes to obtain the best performance. This approach is more like an intermediate stage of applying deep learning since it does not follow the complete end-to-end pattern of deep learning practice[24] but it helped show that value of new deep learning methods for this class of problems. The second approach relies on the encoder-decoder framework to find features[25] in EM images. Examples include using weakly supervised learning methods of encoder-decoder to study the local atom movements[26], U-Net to study nanoparticle segmentations[27], and a modified U-Net framework to segment defects in STEM images of steels[19]. The encoder-decoder framework can extract the most relevant information in images and use the extracted inner state to do other tasks, but the performance of encoder-decoder framework relies on the extracted inner state and good performance requires careful training[25]. The third category of methods are using mature object-detection frameworks, for example, Chen et al. used Mask R-CNN to study the microstructural segmentation of aluminum alloy[28] and Anderson, et al. used Faster R-CNN to study helium bubbles in irradiated X-750 alloy[20]. Here we explore the first use of similar mature object-detection deep learning methods as this third category, specifically Faster R-CNN, to obtain properties of dislocation loops with varying Burgers vector and habit plane in neutron-

irradiation related iron-chromium-aluminum (FeCrAl) materials, These materials are important for the development of next generation nuclear reactors[29–31].

Analyzing the locations and sizes of defects in materials that have undergone irradiation is a widely used application of electron microscopy. In such studies, the key properties are the total number and distribution of each type of defect. Typical defects of interest include grain boundaries, precipitates, dislocation lines, dislocation loops, stacking fault tetrahedra, cavities (voids, bubbles), and co-called "black-spot" defects, which are small defect clusters of interstitials and sometimes vacancies[1,32]. For this study, we focus on the dislocation loops formed within a ferritic alloy, where the loops exist on specific habit planes that manifest themselves with different morphologies due to the projection of a 3D volume imaged using EM[33]. Typical microstructural images of irradiated ferritic steels contain four prominent types of defects: (1) open ellipse loops (single ring edge), (2) open ellipse loops (double ring edges), (3) closed solid elliptical loops, (4) closed circular solid dots[33]. Figure 1 shows a sample STEM image containing all four morphologies of loops obtained from a ferritic alloy irradiated in a materials test reactor. In this paper, we used a modern deep learning-based object detection model called Faster Regional CNN (Faster R-CNN)[34], a widely used deep learning based object detection model[17]. We use the Faster R-CNN to develop an automatic defect detection system for all four morphologies commonly observed in irradiated steels with a body-centered cubic structure and then additional post-processing to analyze their geometrical

information (specifically, size and areal density). This paper serves to demonstrate the power of deep learning-based computer vision models for material image studies and suggests the possibility that most aspects of defect analysis may soon be practically automated, and many, if not all, handcrafted feature-based methods may be replaced by deep learning methods.

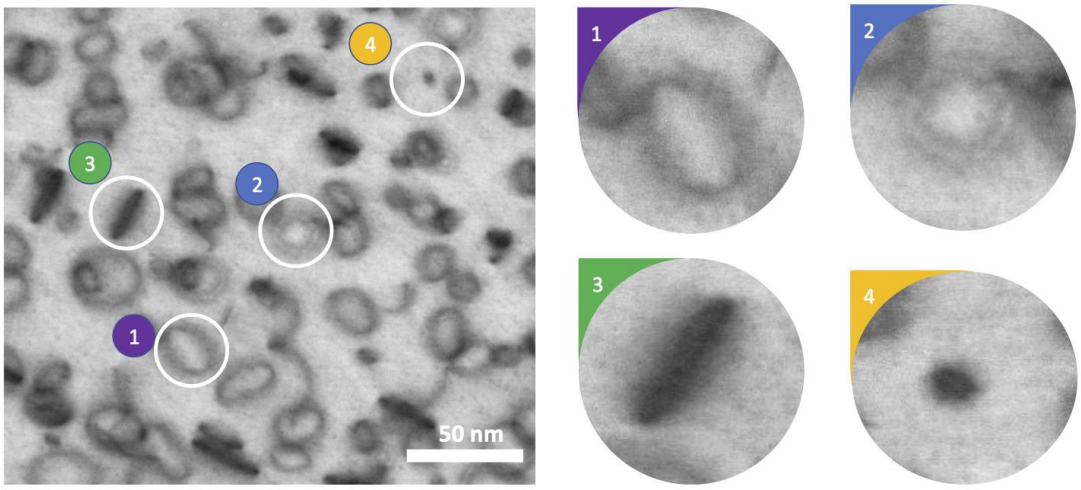

Figure 1. Selected bright field scanning transmission electron microscopy (STEM) image of an irradiated ferritic alloy showing four common morphologies of dislocation loops: (1) open ellipse loops (single ring edge), (2) open ellipse loops (double ring edges), (3) closed elliptical solid loops, (4) closed circular solid dots. Open single edge ellipse loops (1) are dislocation loops with a Burgers vector of $^{a_0}/_2\langle 111\rangle$. Open double edge ellipse loops (2) and closed elliptical solid loops (3) are dislocation loops with a Burgers vector of $a_0\langle 100\rangle$. Closed circular solid dots (4) are black dot defects with a Burgers vector of either $^{a_0}/_2\langle 111\rangle$ or $a_0\langle 100\rangle$. Image size: Primary image is 290 × 290 nm; inset scales arbitrary.

Faster R-CNN is a CNN based end-to-end deep learning object detection model that outputs both the object position and its class[34]. As shown in Figure 2, Faster R-CNN is a two-stage detector where the region proposal network (RPN) proposes Region of Interest (ROI), and the following ROI regressor and classifier will fine tune the final output results including the size and position of the object contained bounding boxes and the corresponding object label[34]. Given an image, the shared convolutional layers will extract a feature map from the input image by performing a series of convolution and max pooling operations. Then based on the extracted feature map, the RPN will put a set of predefined anchor boxes on the feature map and output the probability of whether the anchor box belongs to an object of interest or plain background. It worth mentioning that RPN ignores the specific object class of each bounding box and the following ROI regressor and classifier are responsible for the specific class and refined location of the objects. The refining network predicts certain object labels and refines the size and position of each bounding box based on the feature map generated by the ROI-pooling layers[35]. The RPN and ROI components are trained jointly to minimize the loss function sums from both of them[34]. After the Faster R-CNN module A, those images with detected defects are sent to module B to extract geometric information such as defect diameters, as shown in Figure 2.

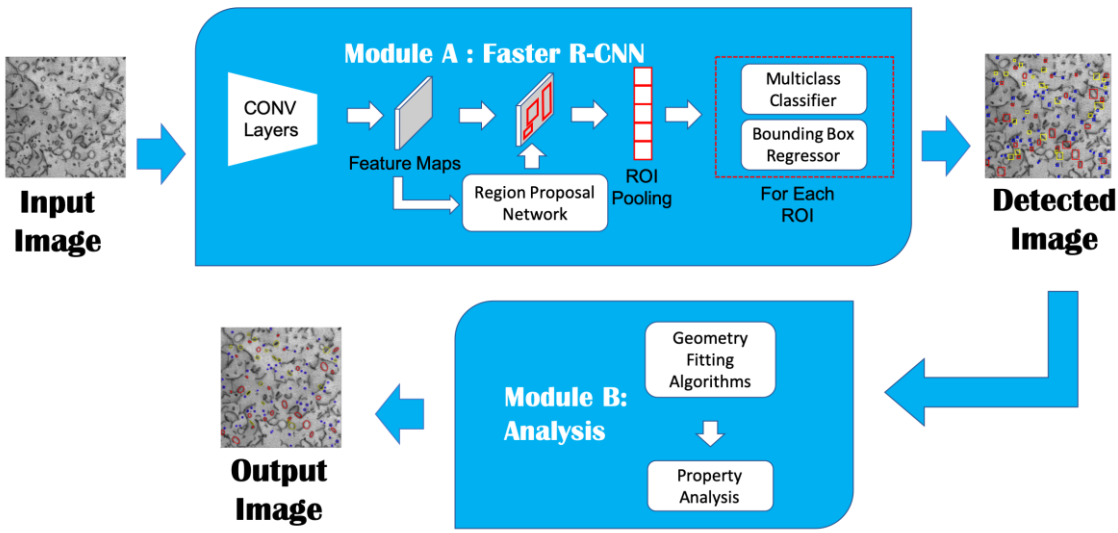

Figure 2. Schematic flow chart of proposed deep learning based automated detection approach. Input micrograph images go through the pipeline of Module A—Faster R-CNN Detector, Module B—Image Property Analysis. After Module A, the loop locations and bounding boxes are identified and then for each identified bounding box, geometry fitting algorithms are called to determine the defect shape and size in Module B.

For details on the data sets, training approaches, and methods of defect identification and analysis, please see Methods section. Please see Data section for summary of all data made available.

RESULTS

To assess the machine predictions, four types of approaches were taken. The first approach was a qualitative comparison of machine to human labeled images, where we looked for large fractions of errors, e.g., more than 40%, and for trends in errors that

might indicate a major issue but made no attempt to quantify agreement. This assessment tests all aspects of the model as it compares to the ground truth human results, which include the bounding box predictions (the defect detection part of Module A in Figure 2), the defect type identifications (the categorization part of Module A in Figure 2), and the geometric shape determination (Module B in Figure 2). The second assessment approach was a quantitative assessment of the ability to identify a defect, regardless of defect types. This assessment tested the defect detection part of Module A (see Figure 2). This assessment was a binary categorization problem and success was quantified with precision, recall, and F1 score. The third assessment was a quantitative assessment of the ability to identify a defect type once a defect had been correctly identified and tested the categorization part of Module A (see Figure 2). This assessment was a three-category categorization problem and was quantified using the confusion matrix with precision, recall and F1 calculated for each class. Finally, the fourth assessment was a quantitative assessment of the ability to quantify the geometric properties of defects. This assessment tested the geometric analysis of Module B (see Figure 2) and compared machine and human predictions of average and standard deviations in size and areal density for each defect type. We discuss each of the four assessments below and label them assessment 1-4 for clarity. In all cases the comparisons are made on the test data set described in Methods section.

Assessment 1. After feeding the images into the Faster R-CNN detectors, the resulting detections were plotted on the original images. As shown in Figure 3, the red circles represent the dislocation loops with a Burgers vector of $a_0/2\langle 111\rangle$ (Type 1 in Figure 1), while the yellow and blue circles represent $a_0\langle 100\rangle$ direction loops (Type 2 and 3 in Figure 1) and "black dot" defects (Type 4 in Figure 1) respectively. The data from both human-labeled and machine detected results are plotted in the same manner. More comparisons can be found in Supplement Information Section 1. To a human observer the machine results show strong correlation of bounding box location, defect type identification, and defect shape with the ground truth human labeling which indicates the effectiveness of the proposed automatic defect detection system.

Assessment 2. The performance of the detection part of Module A (see Figure 2) of the trained model was evaluated in terms of precision, recall, and F1 score by comparing the detected result with the human labeled result of the 12-image testing set, as shown in Figure 4. The precision describes the percentage of all machine predicted bounding boxes that are judged to have correct positions, and the recall value describes the percentage of all human labeled defects that are identified as in a bounding box by the machine algorithm. F1 is the harmonic mean of the precision and recall which can be used to assess the overall performance of the defect location task[35]. The IoU (Intersection over Union) method was used to determine if a given defect was identified by a bounding box and is described within the provided Methods section. The cutoff IoU, which must be

exceeded to consider the bounding box to have identified the defect, is a hyperparameter that can be fine-tuned based on the purpose of the object detection task[35]. Figure 4 showed a drop in performance as the cutoff IoU increased. This trend agreed with expectations as the higher cutoff IoU meant it was harder for the predicted bounding box to be judged successful. However, setting the cutoff IoU to an extremely small threshold could lead to the problem that the predicted bounding boxes are associated with defects for which only a small part of the defect is actually in the bounding box, which will likely cause problems in the defect identification (Module B) of our model. As a compromise, for all the further assessments in this paper, we used cutoff IoU = 0.4 to determine when the machine predictions were considered to match a given defect. This choice kept nearly optimal performance of the detector (based on Figure 4) and an adequately demanding standard for predictions.

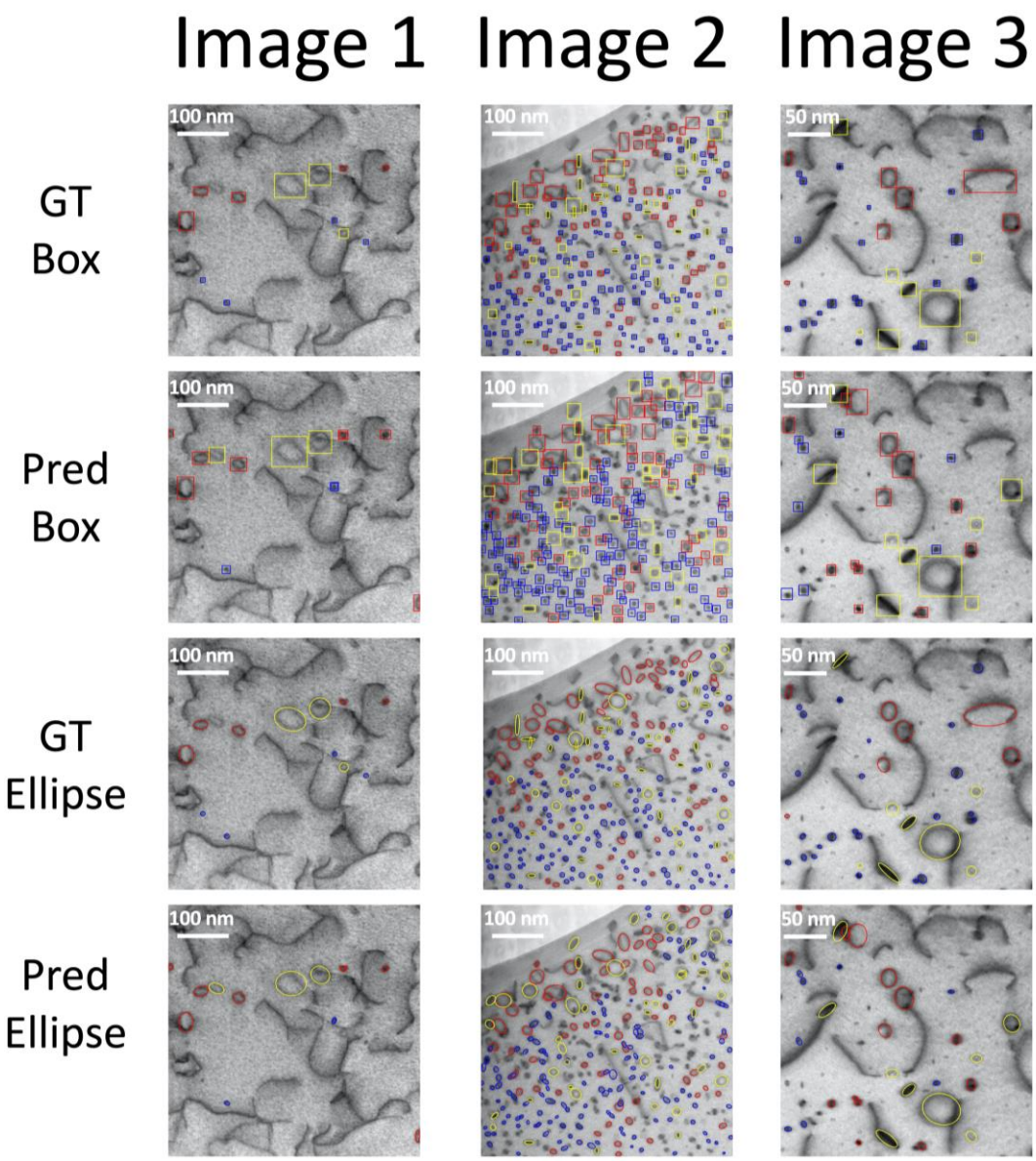

Figure 3.Selected data images to show the detector performance and the fitted ellipse of our automatic analysis system. These three test images are selected from the test dataset of 12 images (see Methods). The "Ground Truth (GT)" shows the bounding box and ellipse human labeling (colored by defect type), the "Prediction (Pred) Box"

shows the predicted bounding boxes (colored by defect type), and the "Prediction (Pred) Ellipse" shows the resulting fits to the specific defect geometry (colored by defect type as described in the text).

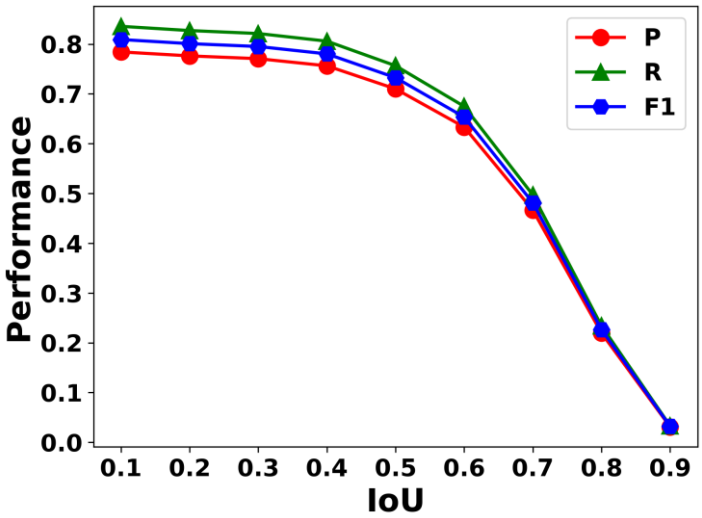

Figure 4. Summary of defect location recognition performance of all types of defects evaluated using precision and recall metrics, regardless of defect types. The test set contained 12 images, and, for all IoU (Intersection over Union) values and we used a threshold confidence score 0.25 for Faster R-CNN output. (see Method Section).

Assessment 3. Table 1 shows the confusion matrix of the predictions made by Faster R-CNN detector evaluating its capability to correctly categorize defects. Each row in the confusion matrix represents a class that is predicted by the detector, and each column represents a class labeled by human researchers. The diagonal elements of the table represent the correct classification made by the detector and off diagonal elements

represent errors of different types. We also show the percentage accuracy of each type of defect in parentheses. The 76%, 87%, and 94% accuracy indicates that once the Faster R-CNN model locates the defect, it can classify the type of defect based on their morphology within the image with good accuracy, although some improvement of the 76% value is likely possible for the $a_0\langle 100\rangle$~~a<100>~~ loops. We also report the classification performance using precision, recall and F1 score in Table 2. Given inherent errors of human performance we take scores for precision, recall and F1 of 0.78 as approximately the upper limit that can be obtained with the present labeling. Table 2 shows F1 from about 0.65 to 0.78, which demonstrates significant capabilities but is likely less than can be achieved, suggesting opportunities for further improvements.

Table 1. Summary of the classification performance for each type of defects at cutoff IoU 0.4. Values in parenthesis give the % each number represents of the total number of defects in that class as determined by the human labeling.

	a_0/2⟨111⟩ Loop	**Black Dot**	**a_0⟨100⟩ Loop**
a/2⟨111⟩ Loop	239 (87.2%)	21	14
Black Dot	17	416 (94.3%)	8
a⟨100⟩ Loop	33	13	166 (78.3%)

Table 2. The performance report for each class.

	a_0/2⟨111⟩ Loop	**Black Dot**	**a_0⟨100⟩ Loop**
Precision	0.73	0.65	0.62
Recall	0.83	0.71	0.72
F1	0.78	0.68	0.67

Assessment 4. The second Module provides geometric in formation for each defect through fitting ellipses. While the fits can provide a range of detailed information, we are particularly interested in the arithmetic mean and the associated standard deviation of the defect diameter as well as the areal density in an image for each type of defect. These values are commonly quoted values in literature within irradiated materials studies. Table 3 compares the human labeled arithmetic mean diameters and areal densities to the ones predicted by the automatic analysis system. The discrepancy of arithmetic mean diameter between the human labeled ground truth and predictions is within 10% in all cases, which is considerably less than might be expected for variation among different humans[2] and we consider a strong success. Furthermore, the errors in arithmetic mean diameters are in the range 0.7-1.1 nm, which corresponds to a range of two to nine pixels (based on the range 0.14nm/pixel to 0.87nm/pixel for our test data, see SI Section 1). The errors of about 1 nm correspond to about 5-10% for our data which is somewhat larger than might be expected from direct labeling errors on 10-15nm. Thus, it is unlikely that any human labeling is meaningfully accurate to much below this level. However, the human and machine learning black dot radii do not fall within a 95% confidence interval, suggesting that the algorithm does not yield exactly the same means as the human ground truth. Some errors will come from the machine detection (failures in precision and recall, see Figure 4) and defect type assignment (see Table 1). Additional errors are associated

with intrinsic errors in the machine and human ellipse labeling, where both have some uncertainty due to ambiguity or variances in the morphology of defects in images. In particular, some defects are not well fit by an ellipse (e.g. some have a more rectangular shape, as can be seen in Figure 3), making this form of labeling difficult for both human and machine. Another error to consider is that as the number of pixels per feature goes down, the intrinsic error due to the resolution (pixel/nm) will artificially go up. For instance, a 100 nm loop where the resolution is 1 pixel/nm where the labeling is off by 1 pixel will yield a 1% error. If the labeling is off by 1 pixel for a 5 nm loop, the error will be 20% even though the per pixel error is the same. Seeing as the black dots are all of small arithmetic mean diameter (<10 nm), they will intrinsically have a higher error compared to the other classes where the diameters are 2-3 times larger.

Table 3. Comparison of arithmetic mean defect diameter and standard deviation of mean loop diameter between ground truth labeling and our automatic analysis model prediction with an IoU of 0.4. The values in parenthesis are the relative percentage error between ground truth human labelling results and the automatic analysis results.

Defect Type	Ground Truth			Automatic Analysis Model		
	Arithmetic Mean diameter (nm)	Standard Deviation of Mean Diameter (nm)	Areal density (m^{-2})	Arithmetic Mean diameter (nm)	Standard Deviation of Mean Diameter (nm)	Areal Density (m^{-2})
$a_0/2$ ⟨111⟩ Loop	22.4	0.7	1.77×10^{14}	23.1 (3.1%)	0.8	2.21×10^{14} (24.9%)
Black Dot	8.2	0.1	3.41×10^{14}	9.1 (10.9%)	0.2	4.98×10^{14} (46.0%)

$a_0\langle 100\rangle$ Loop	20.3	0.8	1.32×10^{14}	22.4 (10.3%)	0.9	1.79×10^{14} (35.6%)

DISCUSSION

The above results demonstrate that that the trained model potentially performs well enough to replace human in a workflow on similar types of data. The precision and recall values for assessing detection in the range 62-83% which are comparable or less than human variation[2] from previous assessments. The machine defect type misidentifications are at the level of 10-25% (see Table 1), and a significant fraction of this variation may also be due to ground truth ambiguities or errors. The final machine predicted diamaters are within a nanometer, approximately 2 pixels in images, which is a level of error that is considered negligible in terms of impact on material properties. To further clarify that the error is negligible for our defect population we have done a sensitivity analysis based on previous studies of hardening from loops. As discussed in Field et al. [31] simple dispersed barrier hardening models suggest that the hardening under irradiation from loops is of the form $\Delta\sigma_y = A\sqrt{d}$ where A is a constant and d is the diameter of the defect. Now consider an error in diameter d defined as ε. The fractional error in $\Delta\sigma_y$ due to the error ε is $\left(\Delta\sigma_y(d+\varepsilon) - \Delta\sigma_y(d)\right)/\Delta\sigma_y(d) \approx \varepsilon/(2d)$, where the approximate equality holds for $\epsilon \ll d$. For ε = 1.7 nm (which is 2 pixels for our largest pixel sizes, see below) and d = 21.4 nm (our average sizes of a/2<111> and a<100> defects), we get the fractional error in $\Delta\sigma_y$ as 1.7 nm / (2 * 21.4 nm) ≈ 0.04, which is well

within the uncertainty of such microstructure-based analysis. However, for smaller defects this percentage error could clearly become larger. The errors of diameter between ML results and human results appear to be approximately symmetrically distributed in positive and negative directions and independent of defect density, as shown in detail in SI section 4 and 5. Furthermore, previous studies indicate that the differences of arithmetic mean diameter between different human labelers can be comparable or larger than values found here between the ML and human results[5]. The discrepancy in areal densities is somewhat larger than might be intuitively expected just from the percentage error in the arithmetic mean diameters. However, additional errors are introduced by the exact definition of areal density (see Methods section) and the additional errors introduced by the imperfect precision and recall.

While the exact performance of the present automated approach compared to different human researchers is difficult to determine rigorously there is no doubt that the present approach is much more consistent. Previous studies have shown that different labelers tend to label defects in different ways and even the same person may label the same defects differently even after a short break[2,5]. Such issues can make any given data analysis somewhat unreliable and make it difficult to integrate results across different teams and or time periods in larger analysis efforts. However, once a machine learning model is properly trained, it will yield a unique and reproducible labeling for every image. If the community could converge on a single or small number of models this

could greatly increase the reproducibility in labeling of STEM experiments. That said, models trained on different data and/or different human labeling could give different predictions, so establishing community accepted models is an important part of using these approaches to obtain more consistent results.

The approach applied here is readily scalable to very large data sets. Analyzing a single image with our model on a reasonable state of the art GPU (NVIDIA's GeForce GTX 1080 GPU) takes about 0.1s, so analyzing all the images in a typical experiment can be done easily in minutes, even less if multiple GPUs are used and as GPU and related processors (e.g., TPU) continue to get faster. As large scale distributed cloud service provider like Google, Amazon and Microsoft are providing cloud service for deep learning applications with GPU machines[36], it would be easy to scale to process even larger amount of data. Furthermore, significant speedup can likely be obtained if desired. We developed the system with the Python code language and the ChainerCV deep learning framework, both of which were chosen for ease of development not for the high-performance in deployment. Replacing Python with C/C++ or using high-performance deep learning frameworks, e.g. Caffe[37], could potentially accelerate the prediction speed of the current model. In particular, the deep learning community is actively designing new methods to accelerate the running speed of model e.g. model compression, weight sharing, or parameter pruning[38] which could also boost the speed of ours. As an example of how fast deep learning AI algorithms can be, researchers from Google have recently

applied deep learning models for cancer diagnosis on data during the actual process of conducting an optical microscopy experiment[39].

The approach applied here is also readily adapted to new defect types and systems. The present model was trained with only a relatively small amount of training data due to the use of transfer learning[40]. With only modest additional data sets (e.g., on the scale of thousands of defects or possibly fewer) and a few rounds of further training as described in Section II of SI, researchers could likely extend the present model to more defects (e.g. separating the two orientations of 111 loops or adding voids, preexisting dislocations, etc.), different imaging conditions (e.g., changes in microscopes, imaging modes, orientation, focus, etc.), and different materials (e.g. other metal alloys).

There are several areas where significant improvements may be obtainable. The first is that the use of real-world data in the study has led to significant time spent labeling and introducing unavoidable human biases and errors into the deep learning model and its assessment. However, it is possible that simulated images could be both more accurately labeled and generated in large volume, potentially allowing much more accurate models to be trained.

The second area where significant improvement is likely is that deep learning methods for object detection continue to evolve rapidly. In particular, deep learning segmentation models[17], which learn a label for every pixel, could be equally or more accurate and remove the step of fitting contours in a bounding box to get geometric

information. Such an approach was applied recently to automatically detect information about dislocation lines, precipitates and voids in STEM images[19].

Conclusion

This study demonstrated a practical deep learning based automatic STEM image defect detection system implemented by incorporating Faster R-CNN for detection and watershed flood algorithm for geometry fitting. Compared with other models proposed before, our model reduced the training effort by utilizing only one module for detection and expanded capability to simultaneously recognize multiple classes of defects. The approach developed here achieved reasonably reliable performance, with an F1 score of 0.78, and predicted sizes and areal densities within the uncertainty of results from human researchers. The automated analysis on NVIDIA's GeForce GTX 1080 GPU processor is about 0.1 s/image, hundreds of times faster than human analysis (≥1 minute/image), and trivially parallelizable and scalable on more processors. The model can also be readily extended to new defects, systems, and conditions with modest training requirements. Thus, our approach provides an accurate, efficient, reproducible, scalable, and extensible method which could replace or greatly enhance human analysis in future studies related to STEM images.

We believe that this framework can be used on many defect and other STEM features simultaneously, eventually providing a general tool for automated analysis across many STEM applications.

METHODS

Data Set Collection

Data set collection was completed as part of a large-scale effort to characterize iron-chromium-aluminum (FeCrAl) materials neutron-irradiated within the High Flux Isotope Reactor at Oak Ridge National Laboratory. The dataset comprises a series of published[29,31,41] and unpublished data. The data collection was completed over 3 years and spaned a range of different FeCrAl alloys, including model, commercial, and engineering-grade alloys irradiated to light water reactor–relevant conditions (e.g., <15 displacements per atom and temperatures of nominally 285–320°C). Images generation are described in more details in Li et al[5].

Data Set Preparation

We used ImageJ[42,43], an open-source software for analysis of scientific images, to manually label all the training and testing data set. And since STEM images are gray scale and ChainerCV[44] expects input images with RGB channels, some modifications are necessary. We use the direct STEM image gray scale for the R channel. Then we use

modifications of the original image gray scale for the G and B channels. Specifically, following Li et al.[5], for G we use a local contrast enhancement of the original gray scale channel saturated to maximum/minimum and for B we use a Gaussian bluer filter of the original gray scale STEM images. For the local contrast enhancement in channel G, we use the Contrast Limited Adaptive Histogram Equalization (CLAHE), a common algorithm used for local contrast enhancement that makes local detail of STEM image enhanced even in regions that are darker or lighter than most of the image. The Gaussian filter used in channel B represents cases where there might be noises or blurring in the STEM images. The parameters used for CLAHE[45] and Gaussian blur[46] are all from the default parameter setting of scikit-images and details can be found in the references given here for these methods. The purpose of adding two more channels in this way is to improve the model performance and make the model more robust by providing more information about various contrast levels or blurring.

For the training and testing on the Faster R-CNN model, a total of 165 STEM images of irradiated ferritic alloys were collected and labeled. The images were taken at different experimental conditions of temperature and irradiation damage level so that the data includes varying defect sizes, shapes, and areal density. We constructed the ground truth labeling by giving each image in the dataset to at least two groups of at least two researchers per group who together labeled each image in that dataset. In some cases, no absolute consensus could be reached on whether a feature was a defect and/or what type

it had, in which case a best effort was made based on group discussion. Details of the protocol are in the SI.

The test dataset was randomly selected from the complete image dataset, so that the training and test were split by approximately 10:1 ratio. The training dataset was then augmented to 918 images in total, which could provide more training instances without spending more manpower on labeling. The data is augmented by rotating and/or flipping each image in the training set, a standard method previously well established to improved results in some cases[47].

Model Training

The Faster R-CNN model used VGG-16 as its backbone architecture and we adopted the module provided by ChainerCV[44] as the Module A in Figure 2 and using watershed function provided by OpenCV[48] as the second module. The initial weights of Faster R-CNN was loaded from the pre-trained weights from ImageNet which is a common practice in the deep learning training strategy[40] called transfer learning. Although ImageNet is trained for image classification, not object detection, there are enough similarities in key features to support effective transfer learning of weights. Transfer learning can reduce the amount of data and training time required for good performance[40]. The Faster R-CNN module was optimized with Stochastic Gradient Descent (SGD) on a single Nvidia GeForce GTX 1080 GPU. The best hyper parameter

set was found by performing hyperparameter search of learning rate from 10^{-3} to 10^{-6} and we adjust the needed iteration numbers correspondingly. The best choice of hyper parameter is a decayed learning rate starting from 10^{-4} and each 20000 iterations the learning rate will decay to one tenth of the previous one. In total 90000 iterations were performed, and a learning loss curve is shown in Figure 5. The geometry extraction module needed no training.

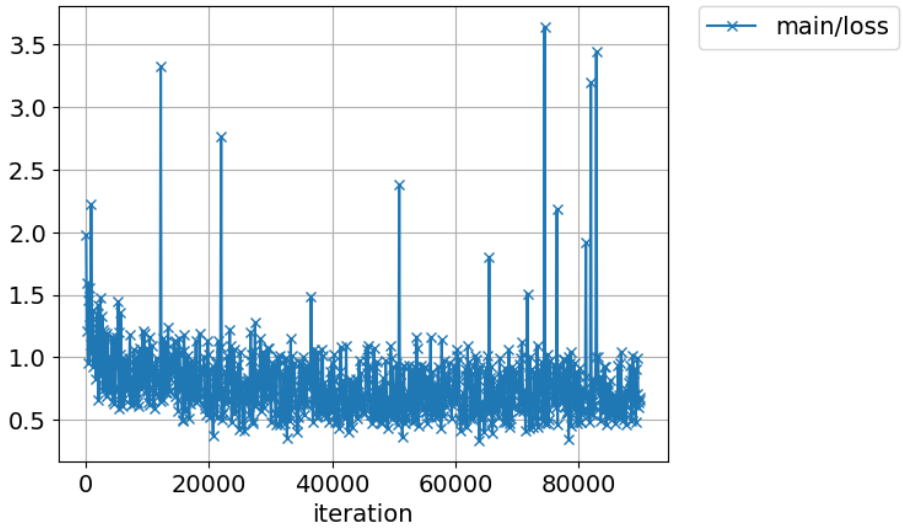

Figure 5. A typical loss curve for Faster R-CNN training.

Model Testing

After the Faster R-CNN module was trained, there were still two important hyperparameter associated with accuracy analysis: the threshold IoU value and the confidence score. IoU stands for Intersection over Union and is an evaluation metric

used to measure the performance of object detection models[17]. IoU is calculated from the ratio of overlap area of a ground truth bounding box and a predicted bounding box to the area of union of two bounding boxes. The range of IoU is from 0 to 1 where 0 means no overlap found between two bounding boxes and 1 means the two bounding boxes are perfectly overlapping. The threshold IoU is the value used to judge the prediction quality of the overlapping of ground truth bounding boxes and prediction bounding boxes. A higher threshold IoU requires more accurate location prediction of the bounding box detector, which will generally reduce performance, but lower the threshold IoU could lead a predicted bounding box to being assigned to no defect or the wrong defect. And another important hyperparameter is the threshold confidence score, a value from 0.0 to 1.0 used by Faster R-CNN internally to discard low confidence proposals in the RPN, and it can change the total number of outputs of Faster R-CNN. We used grid search of the threshold IoU and confidence score to search the best choice of these two values based on maximizing the F1 scores, with confidence score from the list [0.001, 0.005, 0.01, 0.05, 0.1, 0.15, 0.2, 0.25, 0.3, 0.35, 0.4, 0.45, 0.5, 0.55, 0.6] and the threshold IoU from the list [0.1, 0.2, 0.3, 0.4, 0.5, 0.6, 0.7, 0.8, 0.9]. We selected 0.25 as the confidence score for Faster R-CNN and showed the performance changes with 0.4 threshold IoU in Figure 4.

Geometry Fitting of Analysis Module

After the Faster R-CNN module was performed on specific image, the analysis module was called to obtain shape and size of the defect contained in bounding box. As shown in the third column in Figure 3, the approach fits the defect with elliptical contours to estimate their actual shapes and diameters. The approach uses the watershed algorithm to identify the pixels that make up the defect contour and then fit those to an ellipse. The watershed algorithm is a widely used technique for image segmentation purposes that views any gray scale image as a topographic surface where the high (e.g. white) pixel values represents peaks while the low (e.g. black) pixel values denotes valleys. The algorithm tries to grow the region areas by flooding the valleys and where different regions meet with each other are the watershed lines needed for image segmentation[49]. Watershed methods were applied to find the boundary between defect pixels and background pixels. We followed the official tutorial from OpenCV for performing the watershed and details of the approach can be found there[50]. We then fit the boundaries found from the Watershed algorithm to an ellipse. This fitting was done to match the approach used by the radiation defect analysis community, obtain a well-defined shape with simple geometric descriptors, and smooth out the otherwise rather rough boundaries found by the Watershed algorithm. The fitting was done with OpenCV's `fitEllipse()` function[51]. All codes were based with OpenCV[48] and by applying the second module we could get precise information about the defects' position, size, and orientations. The diameters and areas of defects are defined as follows, where *a* and *b* are

half the lengths of major and minor axes of the ellipse. The diameter of the a/2<111> and a<100> defects are defined as 2*a*. The diameter of the black dot is defined as twice the square root of (*ab*). The area of all defects is defined as πab. The areal density is the sum of defect areas in a set of images divided by the total area of the set of images.

Data Availability

We used a subset of published STEM images of the irradiated FeCrAl alloy system[5] (https://publish.globus.org/jspui/handle/ITEM/997) which were labeled and used in this study. The data are available at Figshare (https://doi.org/10.6084/m9.figshare.8266484) and the source code for the model is available on Github (https://github.com/uw-cmg/multitype-defect-detection). The dataset includes both the images and bounding boxes we used for this project. Data on Figshare also includes a CSV file with all data used in plots in this paper.

Supporting Information

We showed the fitting results of all 12 testing images in section 1 of SI. In Section 2 of SI, we presented the labeling process that has been used in a previous study[5] and prepared a detailed instruction document to record our labeling process, which can be easily used for other defect images. In section 3 of SI, detailed statistics distribution of

the human labelling and machine predicting results of diameters and areal density were showed.

Competing Interests:

There are no competing interests in relation to the work described.

Acknowledgments:

We would like to thank Wisconsin Applied Computing Center (WACC) for providing access to CPU/GPU cluster, Euler. And special thanks to Colin Vanden Heuvel for helping us use GPUs and install software needed and sincere thanks to Vanessa Meschke for helping organize the undergraduate students participate in this research in summer 2018.

Funding[1]**:**

Research was sponsored by the Department of Energy (DOE) Office of Nuclear Energy, Advanced Fuel Campaign of the Nuclear Technology Research and Development

[1] Notice: This manuscript has been authored by UT-Battelle, LLC, under contract DE-AC05-00OR22725 with the US Department of Energy (DOE). The US government retains and the publisher, by accepting the article for publication, acknowledges that the US government retains a nonexclusive, paid-up, irrevocable, worldwide license to publish or reproduce the published form of this manuscript, or allow others to do so, for US government purposes. DOE will provide public access to these results of federally sponsored research in accordance with the DOE Public Access Plan (http://energy.gov/downloads/doe-public-access-plan).

program (formerly the Fuel Cycle R&D program). Neutron irradiation of FeCrAl alloys at Oak Ridge National Laboratory's High Flux Isotope Reactor user facility was sponsored by the Scientific User Facilities Division, Office of Basic Energy Sciences, DOE. Support for D. M. was provided by the National Science Foundation Cyberinfrastructure for Sustained Scientific Innovation (CSSI) program, award No. 1931298. Support for select undergraduate participants over some periods provided by the NSF University of Wisconsin-Madison Materials Research Science and Engineering Center (DMR 1720415) and the Schmidt Foundation.

Reference

1. Jenkins, M. . & Kirk, M. . *Characterisation of Radiation Damage by Transmission Electron Microscopy*. *Iop* **20002352**, (Taylor & Francis, 2000).

2. Jesse, S. *et al.* Big Data Analytics for Scanning Transmission Electron Microscopy Ptychography. *Sci. Rep.* **6**, 26348 (2016).

3. Kalinin, S. V., Sumpter, B. G. & Archibald, R. K. Big-deep-smart data in imaging for guiding materials design. *Nat. Mater.* **14**, 973–980 (2015).

4. Duval, L. *et al.* Image processing for materials characterization: Issues, challenges and opportunities. in *2014 IEEE International Conference on Image Processing, ICIP 2014* 4862–4866 (IEEE, 2014). doi:10.1109/ICIP.2014.7025985

5. Li, W., Field, K. G. & Morgan, D. Automated defect analysis in electron microscopic images. *npj Comput. Mater.* **4**, 1–9 (2018).

6. Park, C. & Ding, Y. Automating material image analysis for material discovery. *MRS Commun.* **9**, 545–555 (2019).

7. Groom, D. J. *et al.* Automatic segmentation of inorganic nanoparticles in BF TEM micrographs. *Ultramicroscopy* **194**, 25–34 (2018).

8. DeCost, B. L., Francis, T. & Holm, E. A. Exploring the microstructure manifold: Image texture representations applied to ultrahigh carbon steel microstructures. *Acta Mater.* **133**, 30–40 (2017).

9. Decost, B. L. & Holm, E. A. A computer vision approach for automated analysis

and classification of microstructural image data. *Comput. Mater. Sci.* **110**, 126–133 (2015).

10. DeCost, B. L., Jain, H., Rollett, A. D. & Holm, E. A. Computer Vision and Machine Learning for Autonomous Characterization of AM Powder Feedstocks. *Jom* **69**, 456–465 (2017).

11. DeCost, B. L. & Holm, E. A. Characterizing powder materials using keypoint-based computer vision methods. *Comput. Mater. Sci.* **126**, 438–445 (2017).

12. Marsh, B. P., Chada, N., Sanganna Gari, R. R., Sigdel, K. P. & King, G. M. The Hessian Blob Algorithm: Precise Particle Detection in Atomic Force Microscopy Imagery. *Sci. Rep.* **8**, 978 (2018).

13. Chowdhury, A., Kautz, E., Yener, B. & Lewis, D. Image driven machine learning methods for microstructure recognition. *Comput. Mater. Sci.* **123**, 176–187 (2016).

14. Vlcek, L., Maksov, A., Pan, M., Vasudevan, R. K. & Kalinin, S. V. Knowledge Extraction from Atomically Resolved Images. *ACS Nano* **11**, 10313–10320 (2017).

15. DeCost, B. L. & Holm, E. A. A large dataset of synthetic SEM images of powder materials and their ground truth 3D structures. *Data Br.* **9**, 727–731 (2016).

16. Gola, J. *et al.* Advanced microstructure classification by data mining methods. *Comput. Mater. Sci.* **148**, 324–335 (2018).

17. Liu, L. *et al.* Deep Learning for Generic Object Detection: A Survey. (2018).

18. Zou, Z., Shi, Z., Guo, Y. & Ye, J. Object Detection in 20 Years: A Survey. 1–39

(2019).

19. Roberts, G. *et al.* Deep Learning for Semantic Segmentation of Defects in Advanced STEM Images of Steels. *Sci. Rep.* **9**, (2019).

20. Anderson, C. M., Klein, J., Rajakumar, H., Judge, C. D. & B, L. K. Automated Classification of Helium Ingress in Irradiated X-750. 1–7 (2019).

21. Rusanovsky, M. *et al.* Anomaly Detection using Novel Data Mining and Deep Learning Approach.

22. Ahonen, T., Hadid, A. & Pietikäinen, M. Face description with local binary patterns: Application to face recognition. *IEEE Trans. Pattern Anal. Mach. Intell.* **28**, 2037–2041 (2006).

23. Viola, P. & Jones, M. Rapid object detection using a boosted cascade of simple features. in *Proceedings of the 2001 IEEE Computer Society Conference on Computer Vision and Pattern Recognition. CVPR 2001* **1**, I-511-I–518 (IEEE Comput. Soc).

24. Lecun, Y., Bengio, Y. & Hinton, G. Deep learning. *Nature* **521**, 436–444 (2015).

25. Badrinarayanan, V., Kendall, A. & Cipolla, R. SegNet: A Deep Convolutional Encoder-Decoder Architecture for Image Segmentation. *IEEE Trans. Pattern Anal. Mach. Intell.* **39**, 2481–2495 (2017).

26. Ziatdinov, M. *et al.* Deep Learning of Atomically Resolved Scanning Transmission Electron Microscopy Images: Chemical Identification and Tracking

Local Transformations. *ACS Nano* **11**, 12742–12752 (2017).

27. Zafari, S., Eerola, T., Ferreira, P., Kälviäinen, H. & Bovik, A. Automated Segmentation of Nanoparticles in BF TEM Images by U-Net Binarization and Branch and Bound. in *Lecture Notes in Computer Science (including subseries Lecture Notes in Artificial Intelligence and Lecture Notes in Bioinformatics)* **11678 LNCS**, 113–125 (Springer Verlag, 2019).

28. Chen, D., Zhang, P., Liu, S., Chen, Y. & Zhao, W. Aluminum alloy microstructural segmentation in micrograph with hierarchical parameter transfer learning method. *J. Electron. Imaging* **28**, 1 (2019).

29. Field, K. G., Briggs, S. A., Sridharan, K., Yamamoto, Y. & Howard, R. H. Dislocation loop formation in model FeCrAl alloys after neutron irradiation below 1 dpa. *J. Nucl. Mater.* **495**, 20–26 (2017).

30. Parish, C. M., Field, K. G., Certain, A. G. & Wharry, J. P. Application of STEM characterization for investigating radiation effects in BCC Fe-based alloys. *J. Mater. Res.* **30**, 1275–1289 (2015).

31. Field, K. G., Hu, X., Littrell, K. C., Yamamoto, Y. & Snead, L. L. Radiation tolerance of neutron-irradiated model Fe-Cr-Al alloys. *J. Nucl. Mater.* **465**, 746–755 (2015).

32. Zinkle, S. J. & Busby, J. T. Structural materials for fission & fusion energy. *Materials Today* **12**, 12–19 (2009).

33. Yao, B., Edwards, D. J. & Kurtz, R. J. TEM characterization of dislocation loops in irradiated bcc Fe-based steels. *J. Nucl. Mater.* **434**, 402–410 (2013).

34. Ren, S., He, K., Girshick, R. & Sun, J. Faster R-CNN: Towards Real-Time Object Detection with Region Proposal Networks. *IEEE Trans. Pattern Anal. Mach. Intell.* **39**, 1137–1149 (2015).

35. Zhao, Z.-Q., Zheng, P., Xu, S.-T. & Wu, X. Object Detection With Deep Learning: A Review. *IEEE Trans. Neural Networks Learn. Syst.* 1–21 (2019). doi:10.1109/TNNLS.2018.2876865

36. Dean, J. *et al.* Large Scale Distributed Deep Networks. in *Advances in Neural Information Processing Systems 25* (eds. Pereira, F., Burges, C. J. C., Bottou, L. & Weinberger, K. Q.) 1223–1231 (Curran Associates, Inc., 2012).

37. Jia, Y. *et al.* Caffe. in *Proceedings of the ACM International Conference on Multimedia - MM '14* 675–678 (ACM Press, 2014). doi:10.1145/2647868.2654889

38. Cheng, Y., Wang, D., Zhou, P. & Zhang, T. A Survey of Model Compression and Acceleration for Deep Neural Networks. (2017).

39. Chen, P.-H. C. *et al.* An augmented reality microscope with real-time artificial intelligence integration for cancer diagnosis. *Nat. Med.* 1–5 (2019). doi:10.1038/s41591-019-0539-7

40. Pan, S. J. & Yang, Q. A Survey on Transfer Learning. *IEEE Trans. Knowl. Data Eng.* **22**, 1345–1359 (2010).

41. Field, K. G. *et al.* Heterogeneous dislocation loop formation near grain boundaries in a neutron-irradiated commercial FeCrAl alloy. *J. Nucl. Mater.* **483**, 54–61 (2017).

42. Schindelin, J. *et al.* Fiji: An open-source platform for biological-image analysis. *Nat. Methods* **9**, 676–682 (2012).

43. Schneider, C. A., Rasband, W. S. & Eliceiri, K. W. NIH Image to ImageJ: 25 years of image analysis. *Nat. Methods* **9**, 671–675 (2012).

44. Niitani, Y., Ogawa, T., Saito, S. & Saito, M. ChainerCV: a Library for Deep Learning in Computer Vision. 1217–1220 (2017). doi:10.1145/3123266.3129395

45. Module: exposure — skimage v0.18.0 docs. Available at: https://scikit-image.org/docs/stable/api/skimage.exposure.html#skimage.exposure.equalize_adapthist. (Accessed: 23rd April 2021)

46. Module: filters — skimage v0.19.0.dev0 docs. Available at: https://scikit-image.org/docs/dev/api/skimage.filters.html#skimage.filters.gaussian. (Accessed: 23rd April 2021)

47. Shorten, C. & Khoshgoftaar, T. M. A survey on Image Data Augmentation for Deep Learning. *J. Big Data* **6**, 60 (2019).

48. Garrido, G. & Joshi, P. *OpenCV 3.x with Python By Example Second Edition Make the most of OpenCV and Python to build applications for object recognition and augmented reality*. (2018).

49. Kornilov, A. & Safonov, I. An Overview of Watershed Algorithm Implementations in Open Source Libraries. *J. Imaging* **4**, 123 (2018).

50. OpenCV: Image Segmentation with Watershed Algorithm. Available at: https://docs.opencv.org/master/d3/db4/tutorial_py_watershed.html. (Accessed: 24th March 2021)

51. opencv/fitellipse.py at master · kipr/opencv. Available at: https://github.com/kipr/opencv/blob/master/samples/python/fitellipse.py. (Accessed: 21st April 2021)

CRediT author statement

Mingren Shen: Data Curation, Investigation, Conceptualization, Validation, Visualization, Methodology, Software, Formal analysis, Writing- Original draft, Writing- Reviewing and Editing.
Guanzhao Li: Data Curation, Investigation, Validation.
Dongxia Wu: Data Curation, Investigation, Validation.
Yuhan Liu: Data Curation, Investigation, Validation.
Hima Bharathi Adusumilli: Investigation, Data Curation.
Jacob Greaves: Investigation, Data Curation.
Wei Hao: Investigation, Data Curation.
Nathaniel J. Krakauer: Investigation, Data Curation.
Leah Krudy: Investigation, Data Curation.
Jacob Perez: Investigation, Data Curation.
Varun Sreenivasan: Investigation, Data Curation.
Bryan Sanchez: Investigation, Data Curation.
Oigimer Torres: Investigation, Data Curation.
Wei Li: Conceptualization, Data Curation.
Kevin G. Field: Supervision, Conceptualization, Methodology, Project administration, Funding acquisition, Writing- Reviewing and Editing, Resources.
Dane Morgan: Supervision, Conceptualization, Methodology, Project administration, Funding acquisition, Writing- Reviewing and Editing, Resources.

Declaration of interests

☒ The authors declare that they have no known competing financial interests or personal relationships that could have appeared to influence the work reported in this paper.

☐The authors declare the following financial interests/personal relationships which may be considered as potential competing interests: